

1  
2  
3  
4  
5  
6  
7  
8  
9  
10  
11  
12  
13  
14  
15  
16  
17  
18  
19  
20  
21  
22  
23

**Revision 1**

***Experimental Constraints on Fluid-Rock Reactions During Incipient  
Serpentinization of Harzburgite***

Frieder Klein<sup>1\*</sup>, Niya G. Grozeva<sup>2</sup>, Jeffrey S. Seewald<sup>1</sup>, Thomas M. McCollom<sup>3</sup>, Susan E.  
Humphris<sup>4</sup>, Bruce Moskowitz<sup>5</sup>, Thelma S. Berquó<sup>6</sup>, and Wolf-Achim Kahl<sup>7</sup>

<sup>1</sup>*Department of Marine Chemistry and Geochemistry, Woods Hole Oceanographic  
Institution, Woods Hole, MA 02543, USA*

<sup>2</sup>*Massachusetts Institute of Technology/Woods Hole Oceanographic Institution Joint  
Program in Oceanography, Cambridge, MA 02139, USA*

<sup>3</sup>*Laboratory for Atmospheric and Space Physics, Campus Box 392, University of  
Colorado, Boulder, CO 80309-0392, USA*

<sup>4</sup>*Department of Geology and Geophysics, Woods Hole Oceanographic Institution,  
Woods Hole, MA 02543, USA*

<sup>5</sup>*Department of Earth Sciences, and Institute for Rock Magnetism, University of  
Minnesota, Minneapolis, MN 55455, USA*

<sup>6</sup>*Department of Physics, Concordia College, Moorhead, MN 56562, USA*

<sup>7</sup>*Geosciences Department, University of Bremen, Bremen, 28359, Germany*

*\* corresponding author*

24

## ABSTRACT

25           The exposure of mantle peridotite to water at crustal levels leads to a  
26 cascade of interconnected dissolution-precipitation and reduction-oxidation  
27 reactions - a process referred to as serpentinization. These reactions have major  
28 implications for microbial life through the provision of hydrogen (H<sub>2</sub>). To simulate  
29 incipient serpentinization under well-constrained conditions, we reacted cm-sized  
30 pieces of uncrushed harzburgite with chemically modified seawater at 300°C and 35  
31 MPa for ca. 1.5 years (13441 hours), monitored changes in fluid chemistry over  
32 time, and examined the secondary mineralogy at the termination of the experiment.  
33 Approximately 4 mol % of the protolith underwent alteration forming serpentine,  
34 accessory magnetite, chlorite, and traces of calcite and heazlewoodite. Alteration  
35 textures bear remarkable similarities to those found in partially serpentinized  
36 abyssal peridotites. Neither brucite nor talc precipitated during the experiment.  
37 Given that the starting material contained ~4 times more olivine than  
38 orthopyroxene on a molar basis, mass balance requires that dissolution of  
39 orthopyroxene was significantly faster than dissolution of olivine. Coupled mass  
40 transfer of dissolved Si, Mg, and H<sup>+</sup> between olivine and orthopyroxene reaction  
41 fronts was driven by steep activity gradients and facilitated the precipitation of  
42 serpentine. Hydrogen was released in significant amounts throughout the entire  
43 experiment; however, the H<sub>2</sub> release rate decreased with time. Serpentinization  
44 consumed water but did not release significant amounts of dissolved species (other  
45 than H<sub>2</sub>) suggesting that incipient hydration reactions involved a volume increase of  
46 ~40%. The reduced access of water to fresh olivine surfaces due to filling of

47 fractures and coating of primary minerals with alteration products led to decreased  
48 rates of serpentinization and H<sub>2</sub> release. While this concept might seem at odds with  
49 completely serpentinized seafloor peridotites, reaction-driven fracturing offers an  
50 intriguing solution to the seemingly self-limiting nature of serpentinization. Indeed,  
51 the reacted sample revealed a number of textural features diagnostic of incipient  
52 reaction-driven fracturing. We conclude that fracturing must have far reaching  
53 impacts on the rates of serpentinization and H<sub>2</sub> release in peridotite-hosted  
54 hydrothermal systems.

55

56 **Keywords:** *serpentinization, phase relations, reaction rates, reaction pathways,*  
57 *fracturing, hydrogen, hydrothermal experiment*

58

59

## INTRODUCTION

60 Serpentinization reactions play a prominent role in a wide range of  
61 geophysical, geochemical, and biological processes on Earth, including seafloor  
62 spreading, cycling of water, carbon, and sulfur, abiotic synthesis of organic  
63 compounds, and chemosynthesis (Alt et al., 2013; Escartín et al., 1997; Foustoukos  
64 and Seyfried, 2004; Lang et al., 2010; Schrenk et al., 2013; Schwarzenbach et al.,  
65 2013; Seewald et al., 2006). Serpentinization reactions directly impact the  
66 mechanical properties, magnetic signatures, densities, electrical conductivities, and  
67 trace element contents of ultramafic rocks (Coleman, 1971; Deschamps et al., 2011;  
68 Escartin et al., 2001; Iyer et al., 2008; Jöns et al., 2010; Kelemen and Hirth, 2012;  
69 Kodolanyi et al., 2012; Maffione et al., 2014; Oufi et al., 2002; Paulick et al., 2006;

70 Plümper et al., 2012; Reynard et al., 2011; Stesky and Brace, 1973; Toft et al., 1990).  
71 A key result of serpentinization is the release of H<sub>2</sub> and the creation of chemical  
72 environments that are sufficiently reducing to stabilize native metals and alloys  
73 (Chamberlain et al., 1965) and reduce CO<sub>2</sub> (Foustoukos and Seyfried, 2004; Horita  
74 and Berndt, 1999; McCollom and Seewald, 2001). Moreover, the release of H<sub>2</sub> can  
75 also provide chemolithoautotrophic microorganisms with chemical energy  
76 (Brazelton et al., 2012; Perner et al., 2007; Schrenk et al., 2013).

77         The mechanisms controlling the release of H<sub>2</sub> can be studied in active and  
78 fossil hydrothermal systems, using laboratory experiments, and theoretical models.  
79 Field investigations have highlighted numerous factors that influence the  
80 composition of hydrothermal fluids, such as rock composition, temperature,  
81 pressure, water-to-rock mass ratio, degassing of magmatic volatiles, fluid mixing,  
82 phase separation, stable and metastable fluid-mineral equilibria, reaction kinetics,  
83 porosity, permeability, and biological activity (e.g., Alt and Shanks, 1998; Früh-  
84 Green et al., 2003; Ludwig et al., 2006; Pester et al., 2012; Proskurowski et al., 2006;  
85 Schmidt et al., 2007). Because fluids can integrate a number of individual reactions  
86 involving different rock types along the flow path (Nakamura et al., 2009), chemical  
87 processes during fluid-rock interactions often remain difficult to reconstruct by field  
88 studies alone.

89         Thermodynamic modeling has been used to augment field studies, in  
90 particular to quantify heterogeneous equilibria of complex multi-component  
91 systems (Alt and Shanks, 2003; Bach et al., 2013; Jöns et al., 2010; Klein et al., 2013;  
92 Seyfried et al., 2011; Shock and Canovas, 2010; Sleep et al., 2004; Wetzels and Shock,

93 2000). However, thermodynamic models rely on field observations or laboratory  
94 experiments to constrain kinetically-limited, metastable, and/or permeability-  
95 limited reactions. Laboratory experiments offer the advantage that stable and  
96 metastable phase equilibria, reaction pathways, reaction rates, and many other  
97 parameters can be studied under well-constrained temperature, pressure, and  
98 compositional conditions. Powdered reactants are commonly used in  
99 serpentinization experiments to allow reactions to proceed on laboratory timescales  
100 (e.g., Klein and McCollom, 2013; Malvoisin et al., 2012b; Seyfried and Dibble, 1980).  
101 However, an inherent drawback of powdered reactants is that effects related to  
102 changes in permeability and porosity – key properties in regulating fluid access to  
103 primary mineral surfaces (Godard et al., 2013) – cannot be studied.

104         An intimately linked and still debated question is whether serpentinization is  
105 an isovolumetric process associated with mass transfer or whether it occurs via  
106 simple hydration that requires a volume increase. Isovolumetric serpentinization  
107 implies open system behavior and the removal of Mg, Fe, and Si to accommodate the  
108 uptake of water. Thayer (1966) argued that the preservation of primary textures  
109 such as euhedral olivine pseudomorphs indicates volume-for-volume replacement  
110 and open system behavior (cf. Velbel, 2014). In contrast, Hostetler et al. (1966) and  
111 Page (1967) did not find any field evidence for large-scale removal of Mg or Si.  
112 Isochemical serpentinization (apart from the addition of water) involves large  
113 volume increases, which, depending on the protolith composition can be up to 53%  
114 (O'Hanley, 1992). The resulting decrease in permeability has led some to infer that  
115 serpentinization represents a self-sealing mechanism (Lister, 1974).

116           The concept that serpentinization results in decreased permeability is in  
117 contrast to the high degrees of serpentinization observed in orogenic, ophiolitic, and  
118 abyssal peridotites (Bodinier and Godard, 2007; Dick, 1989). An intriguing  
119 explanation for this observation is persistent reaction-driven fracturing, which may  
120 create new and reactivate existing pathways for fluid transport (Kelemen and Hirth,  
121 2012; Plümper et al., 2012; Rouméjon and Cannat, 2014). Some laboratory  
122 experiments suggest that serpentinization at elevated temperatures is a fast process  
123 on geological timescales (Malvoisin et al., 2012a; Martin and Fyfe, 1970; Wegner and  
124 Ernst, 1983), limited only by water access to primary mineral surfaces (Macdonald  
125 and Fyfe, 1985; Malvoisin and Brunet, 2014). While the use of powdered starting  
126 materials in laboratory serpentinization experiments has provided valuable insight  
127 by allowing reactions to go to completion, this approach does not permit testing of  
128 whether serpentinization is a self-sealing process (Lister, 1974), or whether  
129 serpentinization can go to completion via thermal, tectonic, and reaction-driven  
130 fracturing (Plümper et al., 2012, Rouméjon and Cannat, 2014). Moreover, it remains  
131 unclear how the putative self-sealing nature of serpentinization or fracturing affects  
132 rates of mineral dissolution and H<sub>2</sub> release.

133           With only a few exceptions (e.g., Craddock et al., 2013), abyssal peridotites  
134 are strongly to completely serpentinized (40-100%), making it difficult to study the  
135 earliest stages of serpentinization in seafloor environments. We have conducted an  
136 experimental study to investigate the onset of mineral replacement reactions and  
137 associated changes in fluid chemistry under well-constrained conditions. We  
138 reacted uncrushed harzburgite and modified seawater, monitored changes in fluid

139 chemistry over time, and examined solid reaction products in their textural context.  
140 In addition to providing new insights into reactions taking place during the earliest  
141 stages of serpentinization (cf., Beard et al., 2009; Godard et al., 2013), the results  
142 suggest that H<sub>2</sub> release rates are constrained by water access to primary minerals,  
143 further supporting the idea that continuous fracturing is required for  
144 serpentinization to go to completion.

145

#### 146 **METHODS and MATERIALS**

147 *Experimental setup and analytical techniques* – The experiment was carried out in a  
148 flexible-cell hydrothermal apparatus (Seyfried et al., 1979) consisting of a gold bag  
149 with a titanium closure piece, exit tube, and sampling valve. All Ti surfaces in contact  
150 with the fluid were oxidized in air at 400 °C prior to the experiment to prevent  
151 artificial H<sub>2</sub> release. The flexible reaction cell is enclosed in a stainless steel  
152 pressure-containment vessel filled with water, which acts as the pressure medium.  
153 The flexible gold bag permits external control of pressure and the elimination of a  
154 vapor headspace during the experiment. The titanium sample valve allows periodic  
155 removal of fluid during the experiment for chemical characterization.

156 After loading the reaction cell with 18.19 g of harzburgite and 43.15 g of  
157 evolved seawater (compositional details of starting materials are presented below),  
158 the reaction cell was pressurized to 35MPa and heated to 300°C. When the desired  
159 experimental conditions were reached, the system was allowed to react for 13441 h.

160 Several aliquots (0.3-0.6 g each, ~3 g of fluid in total per sampling event) of  
161 fluid were taken in gas-tight glass syringes on six occasions during the experiment.

162 Quantitative analysis of dissolved H<sub>2</sub> was performed using a gas chromatograph  
163 equipped with a thermal conductivity detector. Dissolved cations were analyzed by  
164 inductively coupled plasma mass spectrometry (Mg) and ion chromatography (Na,  
165 K, Ca). Estimated uncertainties are 2% for Mg, 3% for Na and K, and 5% for Ca.  
166 Dissolved Si was measured spectrophotometrically using the heteropoly-blue  
167 method at a wavelength of 815nm. The estimated uncertainty was 5%. The pH  
168 (25°C) was measured using a micro-combination electrode. The uncertainty was ca.  
169 0.1 unit of the reported value.

170 Polished thin sections of the solid starting material and experimental  
171 reaction products were prepared in oil at High Mesa Petrographics, Los Alamos, NM  
172 to avoid oxidation of Fe(II)-bearing minerals and dissolution of water-soluble  
173 phases. Thin sections were examined optically in transmitted and reflected light  
174 with a petrographic microscope. Backscattered electron images of thin sections and  
175 rock chips were taken with a Hitachi TM3000 scanning electron microscope, the  
176 low-vacuum mode of which permits analysis without carbon coating the sample.  
177 Element distribution mapping was conducted with a Bruker Quantax 70 energy  
178 dispersive X-ray spectrometer coupled to the scanning electron microscope.  
179 Mineral compositions were quantified with a JEOL JXA-8530F 'HyperProbe' Field-  
180 Emission Electron Probe Microanalyzer (Yale University) operated at 15 kV  
181 acceleration voltage and 20nA beam current. The beam was fully focused for  
182 primary silicates and sulfides, but was set to 5-15 μm in diameter for all other  
183 phases to avoid beam damage. Counting times for all elements were 20 seconds  
184 except for F, which was analyzed for 120 seconds. Raw data were corrected using



185 the CITZAF method (Armstrong, 1995). The accuracy and precision of electron  
186 microprobe analysis was ca. 1%.

187         Thin sections and rock chips were analyzed with a Horiba LabRAM HR  
188 confocal Raman spectrometer equipped with a 17 mW 633 nm HeNe laser, an  
189 astigmatic flat field spectrograph with a focal length of 800 mm, and a multichannel  
190 air-cooled (-70 °C) CCD detector. For thin sections, individual spectra were recorded  
191 using a 100x objective with a numerical aperture of 0.9. A grating with 600 grooves  
192 / mm was used for identification of minerals. A confocal hole diameter of 100  $\mu\text{m}$   
193 was chosen for most analyses. Spectra were collected for 5 seconds with 3-5  
194 accumulations between 100  $\text{cm}^{-1}$  and 1300  $\text{cm}^{-1}$ .

195         Magnetic susceptibilities (K) and volumes of solids were measured with a  
196 Bartington MS2B sensor and a Micromeritics AccuPyc II He-pycnometer. The  
197 calibration accuracy for both instruments was 1%. Loss on ignition (LOI) and bulk  
198 rock chemical X-ray fluorescence analysis of powders were carried out at the Peter  
199 Hooper GeoAnalytical Lab at Washington State University, Pullman, WA. The  
200 estimated uncertainty for major elements is on the order of 1%. To quantify the  
201 amount of magnetite present and the distribution, coordination, and oxidation state  
202 of iron in secondary minerals, Mössbauer spectroscopic and magnetization  
203 measurements were conducted at the Institute for Rock Magnetism at the University  
204 of Minnesota (see Klein et al., 2009 for more detailed information).

205

206 *Starting materials* – A peridotite xenolith from the Eifel Volcanic Field (Meerfelder  
207 Maar, Eifel Volcanic Field, Germany) was used for this study to avoid any pre-

208 existing serpentinization of the starting material (Figs. 1, 2). Mass balancing the bulk  
209 major element composition of the starting material as determined with X-ray  
210 fluorescence and electron microprobe analysis (Tables 1, 2) suggests that the  
211 peridotite can be classified as a harzburgite consisting of olivine (~70 wt.%),  
212 orthopyroxene (~25 wt.%), clinopyroxene (~4 wt.%), Cr-spinel (~0.9 wt.%), and  
213 traces (<0.1 wt.%) of amphibole, glass, and primary sulfides. These mineral  
214 abundances are consistent with those estimated from optical thin section and X-ray  
215 microtomography ( $\mu$ -CT) image analysis. However, mineral proportions can vary on  
216 a thin section scale (Fig. 1). All primary silicates are relatively uniform in  
217 composition and do not show any core-to rim variation as determined from electron  
218 microprobe analysis (Table 2). The harzburgite is moderately fractured (Figs. 1 and  
219 2), most likely due to decompression and thermal relaxation during rapid ascent of  
220 the xenolith (cf. Klügel and Klein, 2006). Fracture widths range from < 1 $\mu$ m to 10 $\mu$ m  
221 (Fig. 2).

222 Olivine, orthopyroxene, and clinopyroxene have a Mg# ((mol  
223 MgO/(MgO+FeO)x100) of ~ 91 and NiO, MnO, Al<sub>2</sub>O<sub>3</sub>, Cr<sub>2</sub>O<sub>3</sub>, and CaO contents typical  
224 for these minerals in mantle peridotite (Table 2). Rare amphibole is approximately  
225 of pargasitic composition, has a Mg# of 89, and has slightly elevated contents of K<sub>2</sub>O  
226 and Cr<sub>2</sub>O<sub>3</sub> compared with its ideal end-member. Chromian spinel compositions were  
227 not determined as detailed thin section petrography of the reaction products  
228 revealed that it did not undergo reaction during the experiment. Pentlandite  
229 contains low concentrations of Co (0.6-0.7 wt.%) and Cu (0.1-0.2 wt.%), and Ni is  
230 enriched relative to Fe. The empirical formula of pentlandite in the starting material

231 is  $\text{Ni}_{4.9}\text{Fe}_{4.1}\text{S}_8$ . Pyrrhotite was analyzed semi-quantitatively with energy-dispersive  
232 spectroscopy and is approximately of stoichiometric composition.

233 Olivine and orthopyroxene are anhedral to subhedral with grain diameters  
234 ranging between 0.3 mm and 3.0 mm (average of 1.0 mm) and 0.5 mm and 3.0 mm  
235 (average of 0.8 mm), respectively (Fig. 1). Grain diameters of anhedral to euhedral  
236 clinopyroxene range between 0.05 mm and 1.0 mm (average of 0.4 mm). Weakly  
237 pleochroic anhedral to subhedral amphibole, 0.1-0.2 mm in diameter, occurs in  
238 association with Cr-spinel. It remains unclear whether amphibole is a primary  
239 mineral formed during melt-rock interaction with the volcanic host, or if it formed  
240 as a result of post-magmatic alteration (cf. O'Connor et al., 1996). In some instances,  
241 amphibole is associated with small amounts of light yellow to reddish brown glass  
242 as linings of vugs around spinel, tentatively indicating that it formed during melt-  
243 rock interaction. Detailed thin section analysis did not reveal any phlogopite in the  
244 samples, although traces of Ti-rich phlogopite are present in some mantle xenoliths  
245 from the Meerfelder Maar (Witt-Eickschen et al., 1998).

246 The measured density of the starting material was  $3.326 \text{ g/cm}^3$  and there  
247 was no detectable loss on ignition. While Mössbauer analysis revealed no detectable  
248 Fe(III), the magnetic susceptibility (SI) of the starting material was 12.86,  
249 suggesting that trace amounts of ferromagnetic minerals were present in the  
250 starting material.

251 The harzburgite xenolith was cored with a diamond drill bit and cut with a  
252 diamond saw blade into 6 pieces (each having a volume of  $\sim 1 \text{ cm}^3$ ) to recover fresh

253 cohesive material. The pieces were then thoroughly rinsed in deionized water and  
254 stored in a drying oven at 40 °C until loaded into the hydrothermal apparatus.

255 In the experiment, we reacted the harzburgite with an aqueous fluid of  
256 seawater chlorinity devoid of Mg and SO<sub>4</sub> and enriched in Ca and K (Table 3). This  
257 fluid chemistry was designed to represent seawater that had evolved during low-  
258 temperate alteration of rocks and precipitation of secondary minerals in recharge  
259 zones of mid-ocean ridge environments (Mottl, 1983).

260

261

## RESULTS

262 *Fluid chemistry* - During the course of the experiment, some aqueous species  
263 concentrations remained relatively constant while others were characterized by  
264 relatively large changes (Figure 3 and Table 3). The pH (25 °C) increased from 6.3 at  
265 the beginning of the experiment to 9.0 at its termination. The concentrations of  
266 dissolved Na, K, and Mg did not change significantly with time. In contrast, the  
267 concentration of dissolved Ca decreased from 30.5 to 27.6 mmol/kg during the  
268 experiment. After an initial increase in the concentration of Si from below detection  
269 in the starting fluid to 0.64 mmol/kg in the first sample at 122 h, its concentration  
270 decreased to 0.05 mmol/kg after 13441 hours of reaction.

271 The measured concentration of H<sub>2(aq)</sub> increased to 7.7 mmol/kg by the end of  
272 the experiment; however, the rate of H<sub>2(aq)</sub> concentration increase was not uniform  
273 throughout the experiment (Fig. 4), being fastest early during the experiment and  
274 then decreasing significantly over time.

275

276 *Petrographic observations* - Petrographic observations are summarized in Table 4.  
277 Thin section image analysis of the reacted harzburgite revealed that ~5 vol.% of the  
278 rock consists of secondary minerals formed during the experiment. The extent of  
279 serpentinization was greatest on the exterior rock surface and decreased toward the  
280 center of the rock. Reaction rims around primary minerals on the exterior rock  
281 surface are generally thicker than reaction rims located along internal fractures.  
282 Primary minerals are partly replaced or overgrown by secondary minerals. Primary  
283 silicates, including olivine and orthopyroxene, show abundant indications of  
284 dissolution such as lenticular etch pits, cone-shaped etch pits, en echelon (sawtooth)  
285 etch pits, and denticles (Figs. 5e, 5f, 6e, 6f). Some dissolution features reveal a  
286 preferred orientation and an almost equidistant periodicity (Fig. 6e). In numerous  
287 instances, intragranular fractures initiate at cone-shaped etch pits similar to those  
288 observed in partially serpentinized abyssal peridotite (Figs. 6f, 7f; cf. Klein et al.,  
289 2009; Plümper et al., 2012). Cr-spinel and clinopyroxene do not show any visible  
290 signs of dissolution (Figs. 6c, 7d, 7e).

291         Inspection of the reacted rock exterior revealed a reaction rim consisting of  
292 lizardite + chrysotile ± magnetite ± chlorite ± calcite (Figs. 5, 6). The mineralogy of  
293 the reaction rim varies systematically with its precursor mineral (Fig. 4a). Olivine is  
294 covered by a layer mainly consisting of lizardite intergrown with accessory  
295 magnetite (Fig. 5c, 6a). The latter is also found directly at the olivine surface. In  
296 contrast, lizardite forms a monomineralic layer covering orthopyroxene. In both  
297 instances, the lizardite layer is overgrown by chrysotile, which forms the outermost  
298 layer (Fig. 6a, b, g). Chrysotile is often intergrown with lizardite and minor chlorite

299 forming cactus-like protrusions (Fig. 5a, b). In most areas, the thickness of the  
300 reaction rim around olivine and orthopyroxene varies between 50 and 70 $\mu$ m (Fig.  
301 6a, b, c, g); however, some embayed areas measure up to 0.5 mm. While  
302 clinopyroxene appears to be unaltered, it is in places overgrown by a thin (~5-  
303 10 $\mu$ m) layer of polyhedral serpentine and magnetite filling void spaces overgrown  
304 by chrysotile (Fig. 7d). Lizardite, chrysotile, and polyhedral serpentine form geode-  
305 like compartments on the rock exterior and host sub- to euhedral magnetite (Figs.  
306 5a, c). Chrysotile fibers are about 0.1 to 0.2  $\mu$ m thick and are up to several tens of  $\mu$ m  
307 long (Fig. 5b, 5a, g). Subhedral magnetite, ca. 1  $\mu$ m to 40  $\mu$ m in diameter (Figs. 5, 6),  
308 and euhedral calcite crystals (ca. 5  $\mu$ m to 200 $\mu$ m in diameter, Figs. 5d, 7c), are  
309 embedded in the serpentine matrix. In contrast to magnetite, calcite is found  
310 exclusively on the exterior rock surface. In a few instances, the walls of geode-  
311 shaped features hosted by spinel, clinopyroxene, and accessory amphibole are  
312 coated with euhedral chlorite (Fig. 5g). Chlorite in geodes likely formed at the  
313 expense of amphibole as clinopyroxene and spinel (Fig. 7d, e) appear to be  
314 unaltered.

315         Thin section examination of the rock interior reveals incipient replacement  
316 textures after olivine (mesh texture, Fig. 6d) and orthopyroxene (bastite texture, Fig.  
317 6g). Mesh texture is mainly composed of lizardite and minor magnetite, whereas  
318 brucite is lacking. In numerous instances magnetite formed directly at the olivine  
319 surface (cf. Beard et al., 2009; Frost et al., 2013) during incipient serpentinization  
320 (Figs. 6a, 6b, 6e, 6f, 7e). Bastite texture features intergrowths of lizardite and

321 chlorite, but lacks magnetite and talc. Contacts between mesh and bastite texture  
322 are remarkably sharp (Fig. 6b).

323         The width of veins ranges from  $<1\mu\text{m}$  to  $\sim 100\mu\text{m}$  and decreases away from  
324 the rock surface toward the rock interior (e.g., Fig. 6e). High resolution confocal  
325 Raman spectroscopy revealed that veins cross-cutting olivine are composed of  
326 lizardite (Fig. 8) and accessory magnetite, but lack brucite (cf. Beard et al., 2009;  
327 Frost et al., 2013). Magnetite grains in veins are smaller and less abundant than on  
328 the rock exterior, anhedral and irregularly distributed. They precipitated directly at  
329 the olivine surface and within the serpentine vein matrix. Where an Al- and Si-rich  
330 glassy melt film was present between two adjacent olivine grains (cf. O'Connor et al.,  
331 1996), traces of chlorite formed together with lizardite in the vein center. Veins  
332 cross-cutting pyroxene are composed of lizardite and chlorite. Neither magnetite  
333 nor talc formed at the expense of orthopyroxene.

334         Primary sulfides consisting of pentlandite  $\pm$  pyrrhotite are irregularly  
335 distributed within the rock. Where fluid accessed primary sulfide, heazlewoodite  $\pm$   
336 magnetite precipitated (Fig. 7b). Heazlewoodite is also found in veins and possibly  
337 formed from Ni and S released during dissolution of olivine (Fig. 5f). Pentlandite is  
338 found together with magnetite; however, it remains unclear whether pentlandite  
339 was in equilibrium with magnetite (Fig. 7a). No evidence was found that awaruite, a  
340 common Ni-Fe alloy found in partly altered serpentinite (Klein and Bach, 2009),  
341 formed during the experiment.

342

343 *Composition of secondary minerals* - Lizardite and chrysotile do not reveal  
344 systematic compositional differences that are discernible by electron microprobe  
345 analysis. Conversely, systematic compositional differences exist between serpentine  
346 forming at the expense of olivine and orthopyroxene, and between serpentine from  
347 the exterior rock surface and the interior (Fig. 9, Table 5). On the rock exterior,  
348 serpentine (lizardite and chrysotile) after olivine is on average Fe-poor (Mg# 97),  
349 while serpentine after orthopyroxene is on average richer in Fe (Mg# 95), Al, and Cr.  
350 In contrast, serpentine from the rock interior has lower Mg#s after olivine (~95)  
351 and after orthopyroxene (~92). Serpentine in bastite texture on the exterior rock  
352 surface is depleted in Fe relative to its precursor and forms sharp boundaries with  
353 serpentine after olivine (Fig. 6b). Chlorite has a Mg# of ~90-91 regardless of its  
354 proximity to olivine, orthopyroxene, or the rock exterior. Electron microprobe  
355 analysis of bastite texture in the rock interior revealed substantially higher Al  
356 contents compared with bastite on the rock surface, which can be attributed to  
357 variable contents of chlorite interwoven with serpentine. Magnetite shows  
358 negligible compositional variations with scanning electron microscope energy  
359 dispersive spectroscopy. Heazlewoodite is nearly of end-member composition with  
360 minor impurities of Fe (2.2-3.9 wt.%) and Co (0.25-0.34 wt.%). Calcite is virtually  
361 pure (Table 5) with only traces of MgO (0.04wt.%) and FeO (0.02 wt.%).

362

363 *Magnetite abundance* - The magnetic susceptibility increased from SI ( $\times 10^{-5}$ )= 12.86  
364 to 72.23 and saturation magnetization increased from  $3.4154 \times 10^{-7}$  Am<sup>2</sup> to  $3.431 \times 10^{-5}$   
365 Am<sup>2</sup>, consistent with the precipitation of magnetite during the experiment. No other



366 ferromagnetic minerals were formed. Magnetization measurements suggest that the  
367 bulk rock magnetite content was 0.19 wt.% after 13441 hours of reaction. Because  
368 the bulk sample contained only ~5 vol.% of relatively Fe-poor serpentine and only a  
369 fraction of the Fe in serpentine was ferric, the bulk Fe(III) was below the detection  
370 limit of Mössbauer spectroscopy (~1% bulk Fe(III)).

371

372

### DISCUSSION

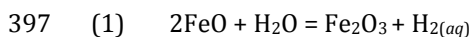
373 *Serpentinization progress* - Serpentinization leads to a decrease in rock density as  
374 higher density primary minerals are replaced with lower density secondary  
375 minerals (except for magnetite, Ni-Fe sulfides and alloys). The extent of  
376 serpentinization can be roughly approximated using the empirical relation  $\rho = 3.30$   
377  $- 0.785S$ , with  $\rho$  being the rock density and  $S$  being the fraction of rock which has  
378 been serpentinized (Miller and Christensen, 1997). During our experiment, the rock  
379 density decreased from an initial value of  $3.326 \text{ g/cm}^3$  to  $3.258 \text{ g/cm}^3$ , which based  
380 on the empirical relation yields  $S \approx 5\%$ .

381 To get an independent estimate for the extent of alteration, we employed a  
382 linear relationship between saturation magnetization ( $J_s$ ) and extent of  
383 serpentinization ( $S$ ):  $J_s = 8.979 \times 10^{-4} \times S$  (Malvoisin et al., 2012b). Using this  
384 relationship, the increase in the measured magnetization saturation during the  
385 experiment,  $J_{s\text{end}} - J_{s\text{initial}} = 3.397 \times 10^{-5} \text{ Am}^2$  suggests that 3.8 % of the protolith  
386 underwent serpentinization.

387 Dissolution rates of primary silicates can be estimated by the release of  
388 elements to solution as a function of time (Wogelius and Walther, 1991). In our

389 experiment, dissolved Mg, Fe, and Si released by dissolution of olivine and  
390 orthopyroxene were immediately consumed during precipitation of serpentine,  
391 magnetite, and chlorite, precluding their use for rate estimates. In contrast, H<sub>2</sub>  
392 released to solution, as Fe(II) in primary minerals was oxidized to Fe(III) in  
393 serpentine and magnetite, is not consumed during mineral precipitation. Therefore,  
394 H<sub>2(aq)</sub> release can be used as an indicator of alteration progress. The generalized  
395 reaction can be represented as:

396



398

399 where FeO and Fe<sub>2</sub>O<sub>3</sub> represent components of primary and secondary minerals,  
400 respectively. Since ferroan brucite did not form during the experiment, the protolith  
401 fraction that underwent serpentinization at the time of fluid sampling can be  
402 estimated. Given that the protolith has an FeO content of ~7.67 wt.% (with  
403 negligible Fe(III) content) (Table 1), and assuming that 2/3 of the Fe in completely  
404 serpentinized peridotite is Fe(III) (Andreani et al., 2013; Klein et al., 2014;  
405 Marcaillou et al., 2011), complete serpentinization of 18.19 g peridotite at the  
406 experimental conditions would release ~ 6.4 mmol H<sub>2(aq)</sub>. After correcting for the  
407 amount of H<sub>2</sub>-bearing fluid removed during each of the six sampling occasions  
408 (Table 3), the total amount of H<sub>2</sub> released after 13441 hours of reaction was 0.24  
409 mmol, suggesting that ~3.8 mol % of the protolith underwent serpentinization. This  
410 value is consistent with the reaction extent estimated from magnetization  
411 saturation measurements. Factoring in a volume increase of 40% during

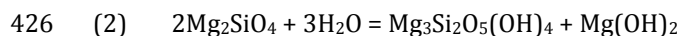
412 serpentinization (see below) these estimates are consistent with thin section  
413 observations, but are slightly lower than density changes would suggest.

414 Most laboratory serpentinization experiments used powdered reactants,  
415 making a straightforward comparison of reaction progress with our estimates  
416 difficult. Malvoisin and Brunet (2014) reacted a sintered San Carlos olivine  
417 aggregate with water at 300°C and 50MPa for 6956 hours. About 2.66 % of the  
418 olivine underwent serpentinization, suggesting that, despite some apparent  
419 differences in protolith composition, overall reaction rates were similar to those in  
420 our experiment.

421

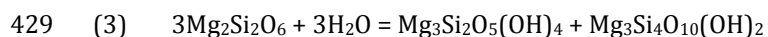
422 *Mass transfer* - Serpentinization involves many chemical components, but the basic  
423 mechanisms can be understood by considering the following reactions in the system  
424 MgO-SiO<sub>2</sub>-H<sub>2</sub>O (Bowen and Tuttle, 1949; Johannes, 1968; Kitahara et al., 1966):

425



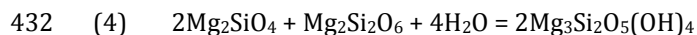
427 forsterite                      serpentine                      brucite

428



430 enstatite                      serpentine                      talc

431

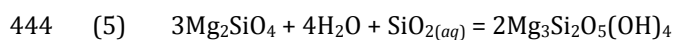


433 forsterite    enstatite                      serpentine

434

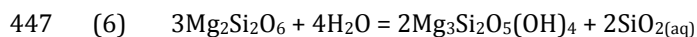
435 In a closed system, serpentinization of forsterite leads to the formation of  
436 serpentine and brucite (2), whereas serpentinization of enstatite leads to the  
437 formation of serpentine and talc (3). If forsterite and enstatite undergo  
438 simultaneous serpentinization at a 2:1 molar ratio, neither brucite nor talc is formed  
439 and the only reaction product is serpentine (4). Indeed, our experiment produced  
440 mainly serpentine without any talc (Fig. 6g) or brucite (Fig. 8) suggesting that  
441 alteration of olivine and orthopyroxene proceeded according to reaction 4. Since  
442 reaction 4 is a composite of reactions:

443



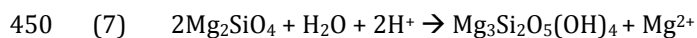
445 forsterite serpentine

446



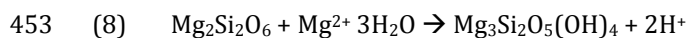
448 enstatite serpentine

449



451 forsterite serpentine

452



454 enstatite serpentine

455

456 it appears that the formation of serpentine involves mass transfers of  $\text{SiO}_{2(aq)}$ ,  $\text{Mg}^{2+}$ ,

457 and  $\text{H}^+$  between the olivine and orthopyroxene reaction fronts. To evaluate mass

458 transfer during the experiment, we calculated the *in situ* speciation of analyzed fluid  
459 compositions using the software code EQ3/6 (Wolery, 1992) and plotted the  
460 computed values in an activity-activity diagram (Fig. 10). This diagram was  
461 constructed using equilibrium constants calculated with the software code  
462 SUPCRT92 (Johnson et al., 1992) and assuming a water activity of 1. Detailed  
463 information about thermodynamic data, activity models, etc. used in the calculations  
464 has been published elsewhere (Klein et al., 2009; 2013; McCollom and Bach, 2009).

465         The main driving force for  $\text{SiO}_{2(aq)}$  mass transfer is a steep activity ( $a$ )  
466 gradient between reactions 5 (equilibrium  $\log a\text{SiO}_{2(aq)} = -5.681$ ) and 6 (equilibrium  
467  $\log a\text{SiO}_{2(aq)} = -0.873$ ) at the experimental conditions. Speciation calculations of *in*  
468 *situ* fluid compositions reveal  $\log a\text{SiO}_{2(aq)}$  values ranging from -3.2 to -4.3, which  
469 plot between reactions 5 and 6 (Fig. 10), consistent with  $\text{SiO}_{2(aq)}$  released by reaction  
470 6 being consumed by reaction 5. As for the steep gradient in  $a\text{SiO}_{2(aq)}$  between  
471 reactions 5 and 6, there are steep gradients in the activities of  $\text{Mg}^{2+}$  and  $\text{H}^+$  (pH)  
472 between reactions 7 and 8. At the experimental conditions, equilibrium values of  
473  $\log(a\text{Mg}^{2+}/a^2\text{H}^+)$  for reactions 7 and 8 are 7.96 and 4.75, respectively, assuming  
474 pure Mg-endmember minerals and a water activity of 1. The calculated *in situ* pH  
475 values ranged between 5.2 and 6.2. Speciation calculations of *in situ* fluid  
476 composition reveal  $\log(a\text{Mg}^{2+}/a^2\text{H}^+)$  values between 5.0 and 6.9, consistent with  
477  $\text{Mg}^{2+}$  released by reaction 7 being consumed by reaction 8, and with  $\text{H}^+$  released by  
478 reaction 8 being consumed by reaction 7. Thus, it appears that mass transfer was  
479 coupled and proceeded in both directions between olivine and orthopyroxene  
480 reaction fronts.

481 Clinopyroxene does not show any obvious signs of dissolution (Figs. 6c, 7d)  
482 suggesting that it did not have a significant impact on mass transfer during the onset  
483 of serpentinization at the experimental conditions.

484 Formation of serpentine according to reaction 4 requires the reaction of 2  
485 moles of forsterite for each mole of enstatite reacted. Because the starting material  
486 had ~4 times more olivine than orthopyroxene on a molar basis, and given that Mg  
487 and Si released during dissolution of both minerals were immediately consumed by  
488 serpentine precipitation, orthopyroxene must have reacted significantly faster than  
489 olivine to fulfill the mass balance. However, since olivine/orthopyroxene mass  
490 ratios vary on a mm to cm scale, it remains difficult to further constrain individual  
491 reaction rates from our experiment.

492

493 *Reaction pathways during serpentinization* - Thermodynamic phase relations suggest  
494 that complete serpentinization of peridotite leads to the formation of serpentine +  
495 brucite ± magnetite (in addition to a number of accessory minerals) (Klein et al.,  
496 2009; Klein et al., 2013; McCollom and Bach, 2009), and that this would have been  
497 the final mineral assemblage had the experiment gone to completion. However, the  
498 experimental results show that incipient serpentinization at the experimental  
499 conditions did not involve the formation of brucite, indicating that serpentinization  
500 must be regarded as a sequence of individual reactions that define a reaction path  
501 (cf. Bach et al., 2004; 2006).

502 As discussed in the previous section, mass balance constraints require that  
503 orthopyroxene dissolution is significantly faster than dissolution of olivine at

504 temperatures of ~300°C. Because orthopyroxene is less abundant than olivine in  
505 peridotite, orthopyroxene will be exhausted from the equilibrium mineral  
506 assemblage first. Once orthopyroxene approaches exhaustion, dissolution of olivine  
507 will dominate and result in the formation of serpentine and brucite (plus magnetite)  
508 as depicted in reaction 2 until olivine is exhausted. The final assemblage of  
509 secondary minerals will therefore include serpentine, brucite, and magnetite (in  
510 addition to traces of other minerals).

511         This reaction path is only valid for temperatures close to 300°C and  
512 peridotite protolith compositions. Serpentinization can take place at temperatures  
513 >350°C, as evidenced by direct temperature measurements of fluids emanating from  
514 the ultramafic-influenced Logatchev, Nibelungen and Rainbow hydrothermal fields  
515 (Douville et al., 2002; Schmidt et al., 2011; Schmidt et al., 2007). Allen and Seyfried  
516 (2003) reacted powdered lherzolite with a NaCl-MgCl<sub>2</sub> bearing fluid at 400°C and 50  
517 MPa for 1462 hours and found that orthopyroxene and clinopyroxene were coated  
518 with alteration products, but olivine surfaces appeared unaltered. Indeed, while it is  
519 predicted that olivine is part of the equilibrium mineral assemblage in the presence  
520 of water at ~400°C (e.g., Klein et al., 2013), orthopyroxene and clinopyroxene are  
521 unstable at these conditions. The reaction pathway of serpentinization at 400°C is  
522 therefore very different from that at 300°C and will be dominated by the  
523 precipitation of serpentine, talc, tremolite and chlorite at the expense of pyroxene.  
524 Once pyroxene is exhausted from the equilibrium mineral assemblage,  
525 serpentinization ceases unless the temperature decreases and olivine becomes  
526 unstable in the presence of water.

527 Lower temperatures of serpentinization of 250°C or less are expected in  
528 areas where magma-supply and thus heat is limited, such as in off-axis  
529 hydrothermal systems like Lost City (Foustoukos et al., 2008; Kelley et al., 2001),  
530 forearc settings of subduction zones (Fryer, 2012), and along magma-poor  
531 continental rifted margins (e.g., Klein et al., 2014). At these temperatures, the  
532 presence of relict orthopyroxene and brucite in the alteration mineral assemblage  
533 may indicate that olivine dissolution was faster than orthopyroxene dissolution (cf.  
534 Martin and Fyfe, 1970). If this is true, then olivine may be consumed during  
535 serpentinization before orthopyroxene. Once olivine approaches exhaustion from  
536 the primary mineral assemblage, the dissolution of remaining orthopyroxene will  
537 dominate the reaction path. Its dissolution provides excess silica, which is available  
538 to react with some of the brucite to form additional serpentine and possibly  
539 magnetite (Bach et al., 2006; Beard et al., 2009). Although the final secondary  
540 mineral assemblage would be the same as that for serpentinization at 300°C, the  
541 pathway is markedly different. It is important to note that magnetite formation is  
542 limited during serpentinization of peridotite at temperatures lower than ~200°C,  
543 because Fe is preferentially taken up by brucite (Klein et al., 2013; 2014; Seyfried et  
544 al., 2007).

545

546 *Serpentinization in different rock domains* –The exterior rock surface and the rock  
547 interior reveal mineralogical, chemical, and textural differences. For example,  
548 secondary minerals on the rock exterior show well-developed crystal habits,  
549 whereas those within the rock do not. Euhedral calcite is present on the rock



550 exterior but did not precipitate in the rock interior. It precipitated from the bulk  
551 solution surrounding the rock, which was apparently saturated with calcite, in  
552 contrast to fluid in the rock interior. It is noteworthy that calcite precipitated at all,  
553 since conditions in the surrounding fluid were relatively reducing. However, it  
554 remains unclear what condition hindered calcite from precipitating within the rock.  
555 Differences in the compositions of serpentine from the rock exterior and interior  
556 (Fig. 9) may reflect distinct fluid-to-rock mass ratios (F/R) and differences in fluid  
557 chemistry. Klein et al. (2009) predicted changes in fluid chemistry, mineralogy, and  
558 mineral chemistry as a function of F/R for serpentinization of harzburgite.  
559 Serpentine is predicted to become richer in Fe with decreasing F/R. Indeed, field  
560 studies suggest that lizardite in veins formed during rock-dominated  
561 serpentinization is Fe-rich relative to chrysotile in veins formed under open system  
562 conditions (Beard et al., 2009; Frost et al., 2013). Chrysotile in the rock exterior may  
563 have formed under similar conditions, with slowly moving or stagnant pore fluids in  
564 fractures. In contrast, serpentinization of the rock interior possibly occurred at  
565 conditions similar to those in rock-dominated domains, away from larger fractures  
566 in hydrothermal systems.

567

568 *Hydrogen release, volume changes, and reaction driven fracturing* - The

569 concentrations of H<sub>2</sub> released during serpentinization have been measured in  
570 several previous laboratory experiments (Allen and Seyfried, 2003; Berndt et al.,  
571 1996; Jones et al., 2010; Klein and McCollom, 2013; Mayhew et al., 2013; McCollom  
572 and Seewald, 2001; Neubeck et al., 2011; Seyfried et al., 2007). Comparison of the

573 results presented here with previous studies at 200 and 400°C conducted in flexible  
574 gold bag reaction vessels show similar temporal trends (Fig. 4). It is important to  
575 note, however, that the absolute values of measured H<sub>2</sub> concentrations are not  
576 directly comparable due to differences in starting materials, grain sizes, fluid-to-  
577 rock mass ratios (F/R), and temperatures. In most experiments, H<sub>2</sub> concentrations  
578 increase with time and extent of serpentinization. There is no clear distinction  
579 between experiments using powdered olivine and peridotite as initial reactants. A  
580 comparison of the H<sub>2</sub> concentrations measured by Berndt et al (1996) and Klein and  
581 McCollom (2013) suggests that the release rate of H<sub>2</sub> is strongly influenced by grain  
582 size (surface area) of the starting materials (cf. Malvoisin et al., 2012b). A common  
583 feature of some experiments is that aqueous H<sub>2</sub> concentrations increase rapidly  
584 shortly after the beginning of an experiment, as primary mineral surfaces are  
585 directly exposed to the interacting fluid. The rate of increase in H<sub>2</sub> concentration  
586 decreases significantly with time. This behavior is most pronounced in our  
587 experiment. The decreased rate of H<sub>2</sub> production cannot be explained with  
588 exhaustion of reactants, because primary silicates were present until the  
589 experiment was terminated. Moreover, olivine and orthopyroxene remained far  
590 from equilibrium throughout the experiment (Fig. 10). Therefore, other mechanisms  
591 must have caused the decreased H<sub>2</sub> release rate. Thin section petrography revealed  
592 filling of fractures and coating of primary mineral surfaces suggesting reduced fluid  
593 access to primary minerals with time and reduced rates of serpentinization and H<sub>2</sub>  
594 generation. Godard et al. (2013) reached similar conclusions based on flow-through  
595 serpentinization experiments that involved sintered olivine as the starting material.

596 In our experiment, serpentinization reactions consumed water but did not  
597 release significant amounts of dissolved species other than H<sub>2</sub>. Thus hydration  
598 reactions must have led to a substantial volume increase. Again, because neither  
599 brucite nor talc formed during the experiment, it follows that incipient  
600 serpentinization was dominated by reaction 4 during our experiment. The volume  
601 increase for this reaction is ca. 40%, which accounts for the observed fracture filling.

602 The self-sealing behavior of serpentinization is at odds with field  
603 observations of high degrees of serpentinization of abyssal peridotites. However,  
604 MacDonald and Fyfe (1985) proposed that volume expansion leads to buildup of  
605 stress and episodic cracking that creates permeability and provides water access to  
606 fresh mineral surfaces. Thin section petrography suggests that grain boundaries and  
607 cracks already present in the protolith (Figs. 1, 2) were preferentially exploited by  
608 serpentinization reactions (cf. Rouméjon and Cannat, 2014). The stress increase due  
609 to volume expansion was sufficient to induce further cracking during our  
610 experiment, in particular along cone-shaped etch pits (e.g., Figs. 6f, 7f). These etch  
611 pits and associated fractures were not observed in the starting material (Fig. 2),  
612 suggesting the creation of new fluid flow paths during the experiment.

613

614

#### **IMPLICATIONS**

615 The results of our laboratory experiment provide new insights into  
616 geochemical processes during incipient serpentinization of peridotite at conditions  
617 representative of hydrothermal seafloor reaction zones. Our experimental  
618 results imply that orthopyroxene reacts significantly faster than olivine at

619 temperatures of ~300°C, which precludes brucite formation early during  
620 serpentinization. This result implies that serpentinization of peridotite at similar  
621 conditions proceeds in two consecutive steps. First, serpentine and minor amounts  
622 of magnetite and chlorite form at the expense of olivine and orthopyroxene. Second,  
623 once the less abundant orthopyroxene approaches exhaustion, dissolution of olivine  
624 will produce serpentine, brucite and magnetite. While this is the same alteration  
625 assemblage produced by serpentinization at lower temperatures, the reaction  
626 pathways are different due to variations in thermodynamic phase relations and  
627 dissolution kinetics of primary minerals.

628         Serpentine precipitation during incipient alteration of peridotite appears to  
629 be mediated by coupled mass transfer of  $\text{SiO}_{2(aq)}$ ,  $\text{Mg}^{2+}$ , and  $\text{H}^+$  along steep activity  
630 gradients between the olivine and orthopyroxene reaction fronts. Dissolved Si and  
631 Mg released during dissolution of olivine and orthopyroxene were consumed by  
632 precipitating serpentine, further supporting the idea that serpentinization can  
633 involve a significant increase in volume and a decrease in permeability.

634         Our experimental results imply that the release rate of  $\text{H}_2$  is limited by water  
635 access to primary mineral surfaces and that serpentinization is, to some extent, a  
636 self-sealing process. However, many abyssal peridotites are strongly fractured and  
637 completely altered suggesting that fracturing promotes water ingress and allows  
638 serpentinization to progress rapidly relative to geological timescales. Fracturing  
639 may therefore have far-reaching implications for the rate of  $\text{H}_2$  production in  
640 subseafloor serpentinization systems.

641

642 *Acknowledgements*

643 This study was partially supported by the National Science Foundation (NSF-OCE  
644 grants 1059534 to F.K. and S.E.H and OCE-0927744 to T.M.M.) and the Deep Ocean  
645 Exploration Institute at the Woods Hole Oceanographic Institution. We thank Sean  
646 Sylva, Margaret Sulanowska, and Jim Eckert for their outstanding support with  
647 sample analysis and Horst Marschall for letting us use his petrographic microscope  
648 and SEM. We also thank Nick Pester, Anna Neubeck, and Associate Editor Dionysis  
649 Foustoukos for helpful and constructive reviews that greatly improved the  
650 manuscript. The IRM is supported by the Instruments and Facilities Program of the  
651 NSF Division of Earth Science. This is IRM contribution 1410.

652

653

654 *Figure captions*

655

656 **Figure 1.** Thin section photomicrograph mosaics of harzburgite used as the starting  
657 material in the experiment in cross-polarized light (left) and plane polarized light  
658 (right). Ol = olivine, Opx = orthopyroxene, Cpx = clinopyroxene, Hbl = hornblende,  
659 Spl = spinel.

660

661 **Figure 2.** Back scattered electron images of the fractured, unaltered protolith.

662 Mineral abbreviations are the same as in Fig. 1.

663

664 **Figure 3.** Changes in fluid chemistry measured during the experiment. Note the  
665 concentration 'breaks' in the ordinate.

666

667 **Figure 4.** Measured  $H_{2(aq)}$  concentrations as a function of time. Hydrogen  
668 concentrations measured during previous experiments are shown for comparison.  
669 F/R = initial fluid to rock mass ratio. See text for discussion.

670

671 **Figure 5.** Back scattered electron images of minerals on exterior surfaces of the  
672 rock after 13441 hours of reaction. (a, b, c) Chrysotile (Ctl), lizardite (Lz), polyhedral  
673 serpentine (P-Srp), and magnetite on relict olivine. Details of (a) are illustrated in  
674 (b) and (c). (d) Euhedral calcite (Cal) and Ctl. (e) Relict orthopyroxene (Opx)  
675 showing abundant dissolution features. (f) Sawtooth vein composed of Lz, magnetite  
676 (Mag), and heazlewoodite (Hzl) cross-cutting relict olivine (Ol). (g) Chlorite (Chl)  
677 geode surrounded by relict clinopyroxene (Cpx), Cr-spinel (Spl), and Ol. (h)  
678 Overview image showing areas depicted in (a, solid white line) and (g, dashed white  
679 line).

680

681 **Figure 6.** Back scattered electron images of thin sections through the rock after  
682 13441 hours of reaction. (a) Overview image of images b (white dashed line) and c  
683 (black dashed line) showing relict Opx and Ol and a typical  $\sim 70$   $\mu\text{m}$  thick reaction  
684 rim at the rock surface composed of Lz + Ctl  $\pm$  Mag. (b) Lz surrounding Opx (light  
685 gray) is significantly richer in Fe than Lz surrounding Ol (dark gray). Fe-rich and Fe-  
686 poor Lz form sharp fronts and are in clear disequilibrium. Note that Mag is found

687 directly at the Ol surface (cf. Beard et al., 2009) and within the reaction rim. (c) Cpx  
688 exsolution lamellae (white) in Opx apparently unaffected by serpentinization. (d)  
689 Incipient formation of pseudomorphic mesh texture along former olivine (sub-)  
690 grain boundaries. (e) Sawtooth vein composed of Lz and minor Mag cross-cutting  
691 relict Ol. (f) Vein composed of Lz and Mag cross-cutting relict Ol. Note the cone-  
692 shaped dissolution features in Ol and extending cracks (white arrow). (g) Mag-free  
693 bastite pseudomorph after Opx. Mineral abbreviations are the same as in Fig. 5.

694

695 **Figure 7.** Back scattered electron images of minor phases (a-c), apparently  
696 unreactive phases (d-e), and an intra-olivine fracture extending from a cone-shaped  
697 etch pit (f). (a) Opaque phase assemblage composed of pentlandite (Pn) and Mag.  
698 (b) Opaque phase assemblage composed of Hzl and Mag. (c) Large subhedral grain  
699 of Cal. (d) Typical Cpx at rock surface with well defined subhedral crystal faces. This  
700 may suggest that Cpx alteration was insignificant. Polyhedral serpentine (P-Srp)  
701 appears to be associated with Cpx, but it remains unclear whether P-Srp formed at  
702 its expense. (e) Unaltered Spl surrounded by partially serpentinized Ol in mesh  
703 texture. (f) Magnified image of cone-shaped etch pit and fracture shown in (e, white  
704 dashed box).

705

706 **Figure 8.** False color Raman map of representative Lz vein (green) cross-cutting  
707 relict Ol (red) within the rock interior. These veins do not host any brucite. Note that  
708 we avoided areas with abundant magnetite for the map. Detailed Raman analysis

709 reveal that, where present, magnetite is not associated with brucite. The spatial  
710 resolution is  $\sim 1\mu\text{m}$ .

711

712 **Figure 9.** Electron microprobe analysis of serpentine after olivine and serpentine-  
713 chlorite intergrowths after orthopyroxene in different rock textures and domains.  
714 The terms 'bastite' and 'mesh' refer to pseudomorphic replacement textures after  
715 orthopyroxene and olivine, respectively.

716

717 **Figure 10.** Activity-activity diagram for the system  $\text{CaO-MgO-SiO}_2\text{-H}_2\text{O}$  at  $300^\circ\text{C}$  and  
718  $35\text{ MPa}$  calculated with the software code SUPCRT92 (Johnson et al., 1992)  
719 assuming  $a_{\text{H}_2\text{O}} = 1$ . The speciated activities of measured fluid compositions fall in  
720 the chrysotile field (representative of serpentine). Sample numbers refer to those  
721 listed in Table 3. The dashed red lines depict the  $\text{SiO}_{2(aq)}$  activities for metastable  
722 equilibrium according to reactions 5 and 6. The blue line denotes the solubility of  
723 quartz. Note that monticellite does not occur in serpentinite. Its formation is  
724 therefore suppressed.



725 **References**

726

- 727 Allen, D. E., and Seyfried, W. E. J. (2003) Compositional controls on vent fluids from  
728 ultramafic-hosted hydrothermal systems at mid-ocean ridges: An experimental  
729 study at 400°C, 500 bars. *Geochimica et Cosmochimica Acta*, 67, 1531-1542.
- 730 Alt, J. C., Schwarzenbach, E. M., Früh-Green, G. L., Shanks Iii, W. C., Bernasconi, S.  
731 M., Garrido, C. J., Crispini, L., Gaggero, L., Padron-Navarta, J. A., and Marchesi,  
732 C. (2013) The role of serpentinites in cycling of carbon and sulfur. *Seafloor*  
733 *serpentinization and subduction metamorphism. Lithos*, 178, 40-54.
- 734 Alt, J. C., and Shanks, W. C., (1998) Sulfur in serpentinitized oceanic peridotites:  
735 Serpentinization processes and microbial sulfate reduction. *Journal of*  
736 *Geophysical Research*, 103, 9917-9929.
- 737 Alt, J. C., and Shanks, W. C. (2003) Serpentinization of abyssal peridotites from the  
738 MARK area, Mid-Atlantic Ridge. Sulfur geochemistry and reaction modeling:  
739 *Geochimica Cosmochimica Acta*, 67, 641-653.
- 740 Andreani, M., Munoz, M., Marcaillou, C., and Delacour, A. (2013)  $\mu$ XANES study of  
741 iron redox state in serpentine during oceanic serpentinization. *Lithos*, 178, 70-83.
- 742 Armstrong, J. T. (1995) CITZAF: A package of correction programs for the quantitative  
743 electron microbeam X-ray analysis of thick polished materials, thin films, and  
744 particles. *Microbeam Analysis*, 4, 177-200.
- 745 Bach, W., Garrido, C. J., Harvey, J., Paulick, H., and Rosner, M. (2004) Seawater-  
746 peridotite interactions – First insights from ODP Leg 209, MAR 15°N.

- 747 Geochemistry, Geophysics, Geosystems 5, Q09F26, doi:  
748 10.1029/2004GC000744.
- 749 Bach, W., Paulick, H., Garrido, C. J., Ildefonse, B., Meurer, W. P., and Humphris, S. E.  
750 (2006) Unraveling the sequence of serpentinization reactions: petrography,  
751 mineral chemistry, and petrophysics of serpentinites from MAR 15°N (ODP Leg  
752 209, Site 1274). Geophysical Research Letters 33, L13306,  
753 doi:10.1029/2006GL025681.
- 754 Bach, W., Jöns, N., and Klein, F. (2013) Metasomatism within the ocean crust. *in*  
755 Metasomatism and the Chemical Transformation of Rock, Halrov, D., and  
756 Austrheim, H., eds., Springer Berlin Heidelberg, 253-288.
- 757 Beard, J. S., Frost, B. R., Fryer, P., McCaig, A., Searle, R., Ildefonse, B., Zinin, P., and  
758 Sharma, S. K. (2009) Onset and progression of serpentinization and magnetite  
759 formation in olivine-rich troctolite from IODP Hole U1309D. *J. Petrology*, 50,  
760 387-403.
- 761 Berndt, M. E., Allen, D. E., and Seyfried, W. E. (1996) Reduction of CO<sub>2</sub> during  
762 serpentinization of olivine at 300°C and 500 bars. *Geology*, 24, 351-354.
- 763 Bodinier, J. L., and Godard, M. (2007) Orogenic, ophiolitic, and abyssal peridotites.  
764 Treatise on Geochemistry: Oxford, Pergamon, 1-73.
- 765 Bowen, N. L., and Tuttle, O. F. (1949) The system MgO-SiO<sub>2</sub>-H<sub>2</sub>O. *Geological Society*  
766 *of America Bulletin*, 60, 439-460.
- 767 Brazelton, W. J., Nelson, B., and Schrenk, M. O. (2012) Metagenomic evidence for H<sub>2</sub>  
768 oxidation and H<sub>2</sub> production by serpentinite-hosted subsurface microbial  
769 communities. *Frontiers in Microbiology*, doi: 10.3389/fmicb.2011.00268.

- 770 Chamberlain, J. A., McLeod, C. R., Traill, R. J., and Lachance, G. R. (1965) Native  
771 metals in the Muskox intrusion. *Canadian Journal of Earth Sciences*, 2, 188-215.
- 772 Coleman, R. G. (1971) Petrologic and geophysical nature of serpentinites. *Geol. Soc.*  
773 *Am. Bull.*, 82, 897-918.
- 774 Craddock, P. R., Warren, J. M., and Dauphas, N. (2013) Abyssal peridotites reveal the  
775 near-chondritic Fe isotopic composition of the Earth. *Earth and Planetary Science*  
776 *Letters*, 365, p. 63-76.
- 777 Deschamps, F., Guillot, S., Godard, M., Andreani, M., and Hattori, K. (2011)  
778 Serpentinites act as sponges for fluid-mobile elements in abyssal and subduction  
779 zone environments. *Terra Nova*, 23, 171-178.
- 780 Dick, H. J. B. (1989) Abyssal peridotites, very slow spreading ridges and ocean ridge  
781 magmatism, *in* Saunders, A. D., and Norry, M. J., eds., *Magmatism in the Ocean*  
782 *Basins*: Oxford, Blackwell, 71-105.
- 783 Douville, E., Charlou, J. L., Oelkers, E. H., Bianvenu, P., Jove Colon, C. F., Donval, J.  
784 P., Fouquet, Y., Prieur, D., and Appriou, P. (2002) The Rainbow vent fluids  
785 (36°14'N, MAR): the influence of ultramafic rocks and phase separation on trace  
786 metal contents on Mid-Atlantic Ridge hydrothermal fluids. *Chemical Geology*,  
787 184, 37-48.
- 788 Escartin, J., Hirth, G., and Evans, B. (2001) Strength of slightly serpentinitized peridotites:  
789 Implications for the tectonics of oceanic lithosphere. *Geology*, 29, 1023-1026.
- 790 Escartín, J., Hirth, G., and Evans, B. (1997) Effects of serpentinitization on the lithospheric  
791 strength and the style of normal faulting at slow-spreading ridges: *Earth and*  
792 *Planetary Science Letters*, 151, 181-189.

- 793 Foustoukos, D. I., Savov, I. P., and Janecky, D. R. (2008) Chemical and isotopic  
794 constraints on water/rock interactions at the Lost City hydrothermal field, 30°N  
795 Mid-Atlantic Ridge. *Geochimica et Cosmochimica Acta*, 72, 5457-5474.
- 796 Foustoukos, D. I., and Seyfried, W. E. (2004) Hydrocarbons in hydrothermal vent fluids.  
797 the role of chromium-bearing catalysts: *Science*, 304, 1002-1005.
- 798 Frost, B. R., Evans, K. A., Swapp, S. M., Beard, J. S., and Mothersole, F. E., (2013) The  
799 process of serpentinization in dunite from New Caledonia. *Lithos*, 24-39.
- 800 Früh-Green, G. L., Kelley, D. S., Bernasconi, S. M., Karson, J. A., Ludwig, K. A.,  
801 Butterfield, D. A., Boschi, C., and Proskurowski, G. (2003) 30,000 years of  
802 hydrothermal activity at the Lost City vent field. *Science*, 301, 495-498.
- 803 Fryer, P. (2012) Serpentinite Mud Volcanism. Observations, Processes, and Implications.  
804 *Annual Review of Marine Science* 4, 345-373.
- 805 Godard, M., Luquot, L., Andreani, M., and Gouze, P. (2013) Incipient hydration of  
806 mantle lithosphere at ridges. A reactive-percolation experiment: *Earth and*  
807 *Planetary Science Letters*, 371, 92-102.
- 808 Horita, J., and Berndt, M. E. (1999) Abiogenic methane formation and isotopic  
809 fractionation under hydrothermal conditions. *Science*, 285, 1055-1057.
- 810 Hostetler, P. B., Coleman, R. G., Mumpton, F. A., and Evans, B. W. (1966) Brucite in  
811 alpine serpentinites. *American Mineralogist*, 51, 75-98.
- 812 Iyer, K., Jamtveit, B., Mathiesen, J., Malthe-Sørenssen, A., and Feder, J. (2008)  
813 Reaction-assisted hierarchical fracturing during serpentinization. *Earth and*  
814 *Planetary Science Letters*, 267, 503-516.

- 815 Johannes, W. (1968) Experimental investigation of the reaction forsterite + H<sub>2</sub>O =  
816 serpentine + brucite. *Contributions to Mineralogy and Petrology*, 19, 305-319.
- 817 Johnson, J. W., Oelkers, E. H., and Helgeson, H. C. (1992) SUPCRT92: A software  
818 package for calculating the standard molal thermodynamic properties of minerals,  
819 gases, aqueous species, and reactions from 1-5000 bars and 0-1000°C. *Computers*  
820 *& Geosciences*, 18, 899-947.
- 821 Jones, L. C., Rosenbauer, R., Goldsmith, J. I., and Oze, C. (2010) Carbonate control of  
822 H<sub>2</sub> and CH<sub>4</sub> production in serpentinization systems at elevated P-Ts. *Geophysical*  
823 *Research Letters*, 37, L14306.
- 824 Jöns, N., Bach, W., and Klein, F. (2010) Magmatic influence on reaction paths and  
825 element transport during serpentinization. *Chemical Geology*, 274, 196-211.
- 826 Kelemen, P. B., and Hirth, G., (2012) Reaction-driven cracking during retrograde  
827 metamorphism: Olivine hydration and carbonation. *Earth and Planetary Science*  
828 *Letters*, 345, 81-89.
- 829 Kelley, D. S., Karson, J. A., Blackman, D. K., Früh-Green, G. L., Butterfield, D. A.,  
830 Lilley, M. D., Olson, E. J., Schrenk, M. O., Roe, K. K., Lebon, G. T., Rivizzigno,  
831 P., and Party, A.-S. (2001) An off-axis hydrothermal vent field near the Mid-  
832 Atlantic Ridge at 30°N. *Nature*, 412, 127-128.
- 833 Kitahara, S., Takenouchi, S., and Kennedy, G. C. (1966) Phase relations in the system  
834 MgO-SiO<sub>2</sub>-H<sub>2</sub>O at high temperatures and pressures. *American Journal of*  
835 *Science*, 264, 223-233.
- 836 Klein, F., and Bach, W. (2009) Fe-Ni-Co-O-S phase relations in peridotite seawater  
837 interactions. *Journal of Petrology*, 50, 37-59.

- 838 Klein, F., Bach, W., Humphris, S. E., Kahl, W.-A., Jöns, N., Moskowitz, B., and Berquó,  
839 T. S. (2014) Magnetite in seafloor serpentinite - Some like it hot. *Geology*, 42,  
840 135-138.
- 841 Klein, F., Bach, W., Jöns, N., McCollom, T., Moskowitz, B., and Berquó, T. (2009) Iron  
842 partitioning and hydrogen generation during serpentinization of abyssal  
843 peridotites from 15°N on the Mid-Atlantic Ridge. *Geochimica et Cosmochimica*  
844 *Acta*, 73, 6868-6893.
- 845 Klein, F., Bach, W., and McCollom, T. M. (2013) Compositional controls on hydrogen  
846 generation during serpentinization of ultramafic rocks. *Lithos*, 178, 55-69.
- 847 Klein, F., and McCollom, T. M. (2013) From serpentinization to carbonation: New  
848 insights from a CO<sub>2</sub> injection experiment. *Earth and Planetary Science Letters*,  
849 379, 137-145.
- 850 Klügel, A., and Klein, F. (2006) Complex magma storage and ascent at embryonic  
851 submarine volcanoes from the Madeira Archipelago. *Geology*, 34, 337-340.
- 852 Kodolanyi, J., Pettke, T., Spandler, C., Kamber, B. S., and Gmeling, K. (2012)  
853 Geochemistry of ocean floor and fore-arc serpentinites: constraints on the  
854 ultramafic input to subduction zones. *Journal of Petrology*, 53, 235-270.
- 855 Lang, S. Q., Butterfield, D. A., Schulte, M., Kelley, D. S., and Lilley, M. D. (2010)  
856 Elevated concentrations of formate, acetate and dissolved organic carbon found at  
857 the Lost City hydrothermal field. *Geochimica et Cosmochimica Acta*, 74, 941-  
858 952.
- 859 Lister, C. R. B. (1974) On the penetration of water into hot rock. *Geophysical Journal of*  
860 *the Royal Astronomical Society*, 39, 465-509.

- 861 Ludwig, K. A., Kelley, D. S., Butterfield, D. A., Nelson, B. K., and Früh-Green, G.  
862 (2006) Formation and evolution of carbonate chimneys at the Lost City  
863 Hydrothermal Field. *Geochimica et Cosmochimica Acta*, 70, 3625-3645.
- 864 Macdonald, A. H., and Fyfe, W. S. (1985) Rate of serpentinization in seafloor  
865 environments. *Tectonophysics*, 116, 123-135.
- 866 Maffione, M., Morris, A., Plümper, O., and van Hinsbergen, D. J. J. (2014) Magnetic  
867 properties of variably serpentinized peridotites and their implication for the  
868 evolution of oceanic core complexes. *Geochemistry, Geophysics, Geosystems*,  
869 15, 923-944.
- 870 Malvoisin, B. and Brunet, F. (2014). Water diffusion-transport in a synthetic dunite:  
871 Consequences for oceanic peridotite serpentinization. *Earth and Planetary Science*  
872 *Letters* 403, 263-272, 10.1016/j.epsl.2014.07.004.
- 873 Malvoisin, B., Brunet, F., Carlut, J., Rouméjon, S., and Cannat, M. (2012a)  
874 Serpentinization of oceanic peridotites: 2. Kinetics and processes of San Carlos  
875 olivine hydrothermal alteration. *Journal of Geophysical Research*, 117, B04102.
- 876 Malvoisin, B., Carlut, J., and Brunet, F. (2012b) Serpentinization of oceanic peridotites:  
877 1. A high-sensitivity method to monitor magnetite production in hydrothermal  
878 experiments. *Journal of Geophysical Research*, 117, B01104.
- 879 Martin, B., and Fyfe, W. S. (1970) Some experimental and theoretical observations on  
880 the kinetics of hydration reactions with particular reference to serpentinization.  
881 *Chemical Geology*, 6, 185-202.

- 882 Mayhew, L. E., Ellison, E. T., McCollom, T. M., Trainor, T. P., and Templeton, A. S.  
883 (2013) Hydrogen generation from low-temperature water-rock reactions. *Nature*,  
884 6, 478-484.
- 885 McCollom, T. M., and Bach, W. (2009) Thermodynamic constraints on hydrogen  
886 generation during serpentinization of ultramafic rocks. *Geochimica et*  
887 *Cosmochimica Acta*, 73, 856-875.
- 888 McCollom, T. M., and Seewald, J. S. (2001) A reassessment of the potential for reduction  
889 of dissolved CO<sub>2</sub> to hydrocarbons during serpentinization of olivine. *Geochimica*  
890 *et Cosmochimica Acta*, 65, 3769-3778.
- 891 Miller, D. J., and Christensen, N. I. (1997) Seismic velocities of lower crustal and upper  
892 mantle rocks from the slow-spreading Mid-Atlantic Ridge, south of the Kane  
893 transform zone (MARK). *Proceedings of the Ocean Drilling Program Scientific*  
894 *Results*, 153, 437-454.
- 895 Mottl, M. J. (1983) Metabasalts, axial hot springs, and the structure of hydrothermal  
896 systems at mid-ocean ridges. *Geological Society of America Bulletin*, 94, 161-  
897 180.
- 898 Nakamura, K., Morishita, T., Bach, W., Klein, F., Hara, K., Okino, K., Takai, K., and  
899 Kumagai, H. (2009) Serpentinized troctolites exposed near the Kairei  
900 Hydrothermal Field, Central Indian Ridge: Insights into the origin of the Kairei  
901 hydrothermal fluid supporting a unique microbial ecosystem. *Earth and Planetary*  
902 *Science Letters*, 280, 128-136.



- 903 Neubeck, A., Duc, N., Bastviken, D., Crill, P., and Holm, N. (2011) Formation of H<sub>2</sub> and  
904 CH<sub>4</sub> by weathering of olivine at temperatures between 30 and 70°C. *Geochemical*  
905 *Transactions*, 12, 6.
- 906 O'Connor, T. K., Edgar, A. D., and Lloyd, F. E. (1996) Origin of glass in Quaternary  
907 mantle xenoliths from Meerfeldermaar, West Eifel, Germany: implications for  
908 enrichment in the lithospheric mantle. *Canadian Mineralogist*, 34, 187-200.
- 909 O'Hanley, D. S. (1992) Solution to the volume problem in serpentinization. *Geology*, 20,  
910 705-708.
- 911 Oufi, O., Cannat, M., and Horen, H. (2002) Magnetic properties of variably serpentinized  
912 abyssal peridotite. *Journal of Geophysical Research*, 107,  
913 10.1029/2001JB000549.
- 914 Page, N. J. (1967) Serpentinization at Burro Mountain, California. *Contributions to*  
915 *Mineralogy and Petrology*, 14, 321-342.
- 916 Paulick, H., Bach, W., Godard, M., de Hoog, J. C. M., Suhr, G., and Harvey, J. (2006)  
917 Geochemistry of abyssal peridotites (Mid-Atlantic Ridge, 15°20'N, ODP Leg  
918 209): implications for fluid-rock interaction in slow spreading environments.  
919 *Chemical Geology*, 234, 179-210.
- 920 Perner, M., Kuever, J., Seifert, R., Pape, T., Koschinsky, A., Schmidt, K., Strauss, H.,  
921 and Imhoff, J. F. (2007) The influence of ultramafic rocks on microbial  
922 communities at the Logatchev hydrothermal field, located 15°N on the Mid-  
923 Atlantic Ridge. *FEMS Microbiology Ecology*, 61, 97-109.
- 924 Pester, N. J., Reeves, E. P., Rough, M. E., Ding, K., Seewald, J. S., and Seyfried Jr, W. E.  
925 (2012) Subseafloor phase equilibria in high-temperature hydrothermal fluids of

- 926 the Lucky Strike Seamount (Mid-Atlantic Ridge, 37°N). *Geochimica et*  
927 *Cosmochimica Acta*, 90, 303-322.
- 928 Plümpner, O., Røyne, A., Magrasó, A., and Jamtveit, B. (2012) The interface-scale  
929 mechanism of reaction-induced fracturing during serpentinization. *Geology*,  
930 10.1130/G33390.1.
- 931 Proskurowski, G., Lilley, M. D., Kelley, D. S., and Olson, E. J. (2006) Low temperature  
932 volatile production at the Lost City hydrothermal field, evidence from a hydrogen  
933 stable isotope geothermometer. *Chemical Geology*, 229, 331-343.
- 934 Reynard, B., Mibe, K., and de Moortelèle, B. V. (2011) Electrical conductivity of the  
935 serpentinised mantle and fluid flow in subduction zones. *Earth and Planetary*  
936 *Science Letters*, 307, 387-394.
- 937 Rouméjon, S. and Cannat, M. (2014) Serpentinization of mantle-derived peridotites  
938 at mid-ocean ridges: Mesh texture development in the context of tectonic  
939 exhumation. *Geochemistry, Geophysics, Geosystems* 15, 2354-2379,  
940 10.1002/2013gc005148.
- 941 Schmidt, K., Garbe-Schönberg, D., Koschinsky, A., Strauss, H., Jost, C. L., Klevenz, V.,  
942 and Königer, P. (2011) Fluid elemental and stable isotope composition of the  
943 Nibelungen hydrothermal field (8°18'S, Mid-Atlantic Ridge): Constraints on  
944 fluid-rock interaction in heterogeneous lithosphere. *Chemical Geology*, 280, 1-18.
- 945 Schmidt, K., Koschinsky, A., Garbe, S. D., de Carvalho, L. M., and Seifert, R. (2007)  
946 Geochemistry of hydrothermal fluids from the ultramafic-hosted Logatchev  
947 hydrothermal field, 15°N on the Mid-Atlantic Ridge: temporal and spatial  
948 investigation. *Chemical Geology*, 242, 1-21.

- 949 Schrenk, M. O., Brazelton, W. J., and Lang, S. Q. (2013) Serpentinization, carbon, and  
950 deep life. *Reviews in Mineralogy and Geochemistry*, 75, 575-606.
- 951 Schwarzenbach, E. M., Früh-Green, G. L., Bernasconi, S. M., Alt, J. C., and Plas, A.  
952 (2013) Serpentinization and carbon sequestration: A study of two ancient  
953 peridotite-hosted hydrothermal systems. *Chemical Geology*, 351, 115-133.
- 954 Seewald, J. S., Zolotov, M. Y., and McCollom, T. (2006) Experimental investigation of  
955 single carbon compounds under hydrothermal conditions. *Geochimica et*  
956 *Cosmochimica Acta*, 70, 446-460.
- 957 Seyfried, W. E., and Dibble, W. E. J. (1980) Seawater-peridotite interaction at 300 °C  
958 and 500 bars: implications for the origin of oceanic serpentinites. *Geochimica et*  
959 *Cosmochimica Acta*, 44, 309-321.
- 960 Seyfried, W. E., Jr., Foustoukos, D. I., and Fu, Q. (2007) Redox evolution and mass  
961 transfer during serpentinization; an experimental and theoretical study at 200 °C,  
962 500 bar with implications for ultramafic-hosted hydrothermal systems at mid-  
963 ocean ridges. *Geochimica et Cosmochimica Acta*, 71, 3872-3886.
- 964 Seyfried, W. E., Jr., Gordon, P. C., and Dickson, F. W. (1979) A new reaction cell for  
965 hydrothermal solution equipment. *American Mineralogist*, 64, 646-649.
- 966 Seyfried, W. E., Pester, N. J., Ding, K., and Rough, M. (2011) Vent fluid chemistry of the  
967 Rainbow hydrothermal system (36°N, MAR): Phase equilibria and in situ pH  
968 controls on subseafloor alteration processes. *Geochimica et Cosmochimica Acta*,  
969 75, 1574-1593.
- 970 Shock, E., and Canovas, P. (2010) The potential for abiotic organic synthesis and  
971 biosynthesis at seafloor hydrothermal systems. *Geofluids*, 10, 161-192.

- 972 Sleep, N., Meibom, A., Fridriksson, T., Coleman, R., and Bird, D. (2004) H<sub>2</sub>-rich fluids  
973 from serpentinization: Geochemical and biotic implications. Proceedings of the  
974 National Academy of Sciences, 101, 12818 - 12823.
- 975 Stesky, R. M., and Brace, W. F. (1973) Electrical conductivity of serpentinized rocks to 6  
976 kilobars. Journal of Geophysical Research, 78, 7614-7621.
- 977 Thayer, T. P. (1966) Serpentinization considered as a constant-volume metasomatic  
978 process. American Mineralogist, 51, 685-710.
- 979 Toft, P. B., Arkani-Hamed, J., and Haggerty, S. E. (1990) The effects of serpentinization  
980 on density and magnetic susceptibility: a petrophysical model. Physics of the  
981 Earth and Planetary Interiors, 65, 137-157.
- 982 Velbel, M. A. (2014) Stoichiometric reactions describing serpentinization of anhydrous  
983 primary silicates: a critical appraisal, with application to aqueous alteration of  
984 chondrule silicates in CM carbonaceous chondrites. Clays and Clay Minerals 62,  
985 126-136.
- 986 Wegner, W. W., and Ernst, W. G. (1983) Experimentally determined hydration and  
987 dehydration reactions rates in the system MgO-SiO<sub>2</sub>-H<sub>2</sub>O. American Journal of  
988 Science, 283, 151-180.
- 989 Wetzel, L. R., and Shock, E. L. (2000) Distinguishing ultramafic- from basalt-hosted  
990 submarine hydrothermal systems by comparing calculated vent fluid  
991 compositions. Journal of Geophysical Research, 105, 8319-8340.
- 992 Whitney, D. L. and Evans, B. W. (2010) Abbreviations for names of rock-forming  
993 minerals. *American Mineralogist* 95, 185-187.

- 994 Witt-Eickschen, G., Kaminsky, W., Kramm, U., and Harte, B. (1998) The Nature of  
995 Young Vein Metasomatism in the Lithosphere of the West Eifel (Germany):  
996 Geochemical and Isotopic Constraints from Composite Mantle Xenoliths from the  
997 Meerfelder Maar. *Journal of Petrology*, 39, 155-185.
- 998 Wogelius, R. A., and Walther, J. V. (1991) Olivine dissolution at 25°C: Effects of pH,  
999 CO<sub>2</sub>, and organic acids. *Geochimica et Cosmochimica Acta*, 55, 943-954.
- 1000 Wolery, T. J. (1992) EQ3NR, A Computer Program for Geochemical Aqueous  
1001 Speciation-Solubility Calculations: Theoretical Manual, User's Guide, and  
1002 Related Documentation (Version 7.0), Lawrence Livermore National Laboratory.  
1003

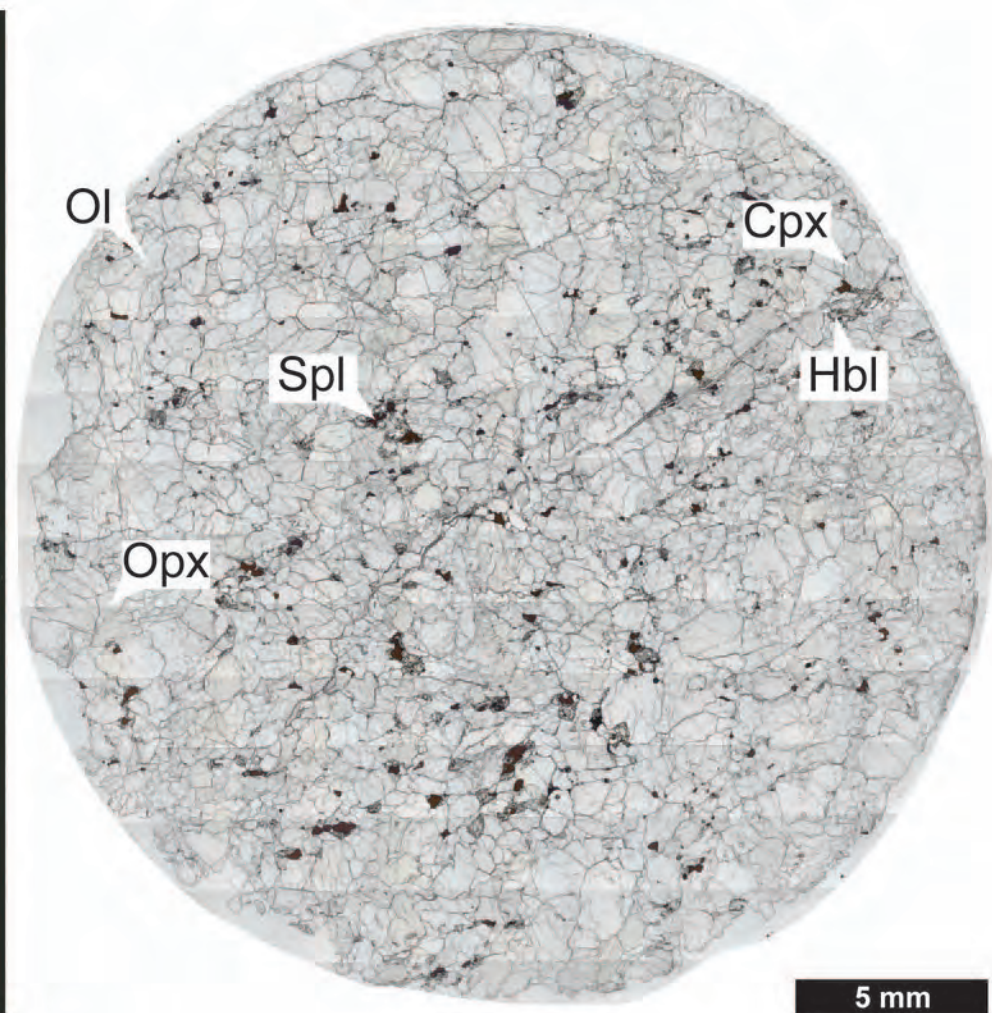
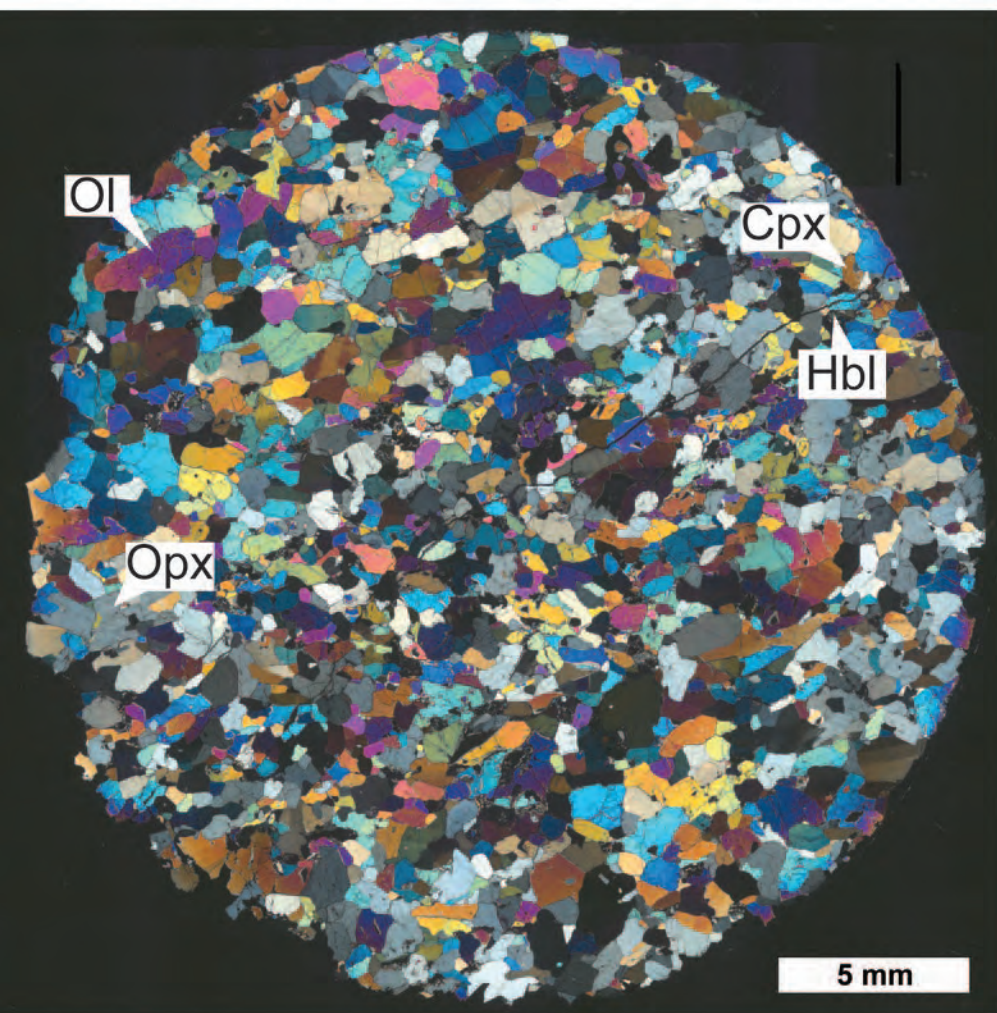


Figure 1

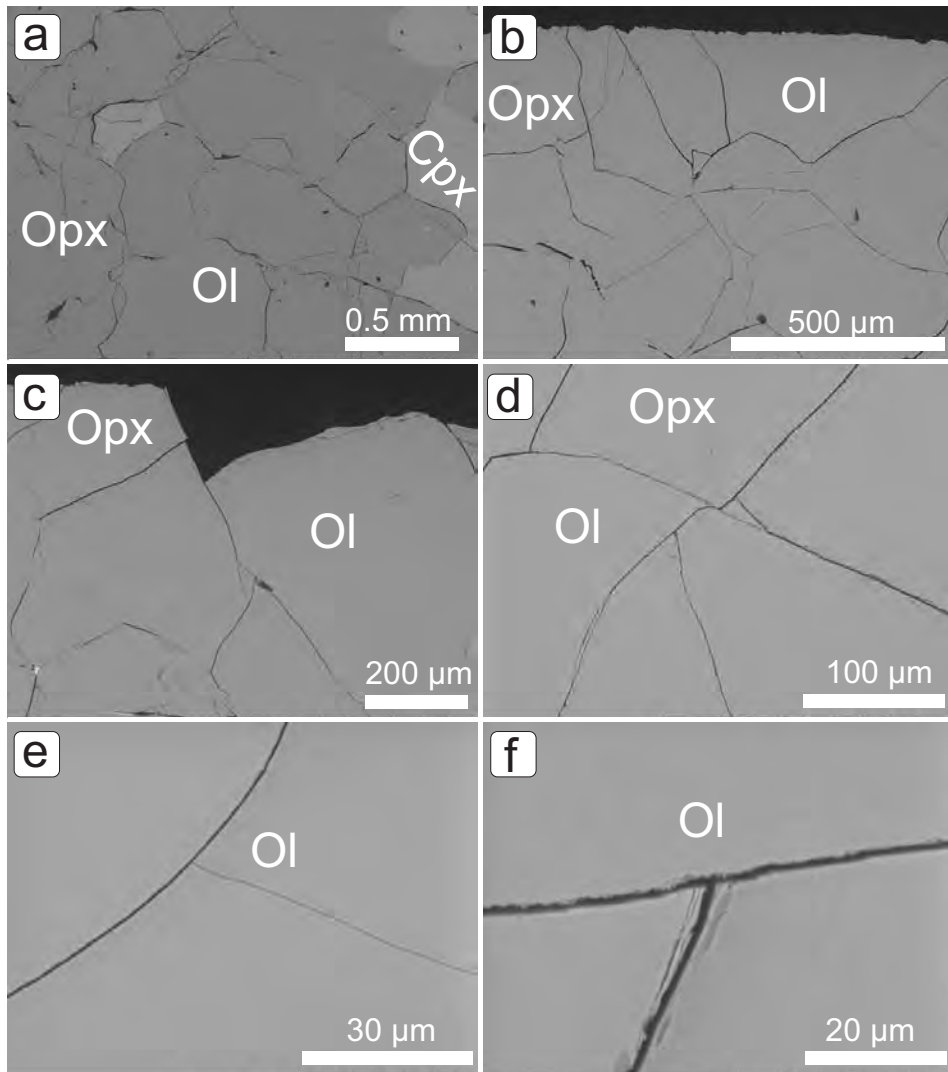
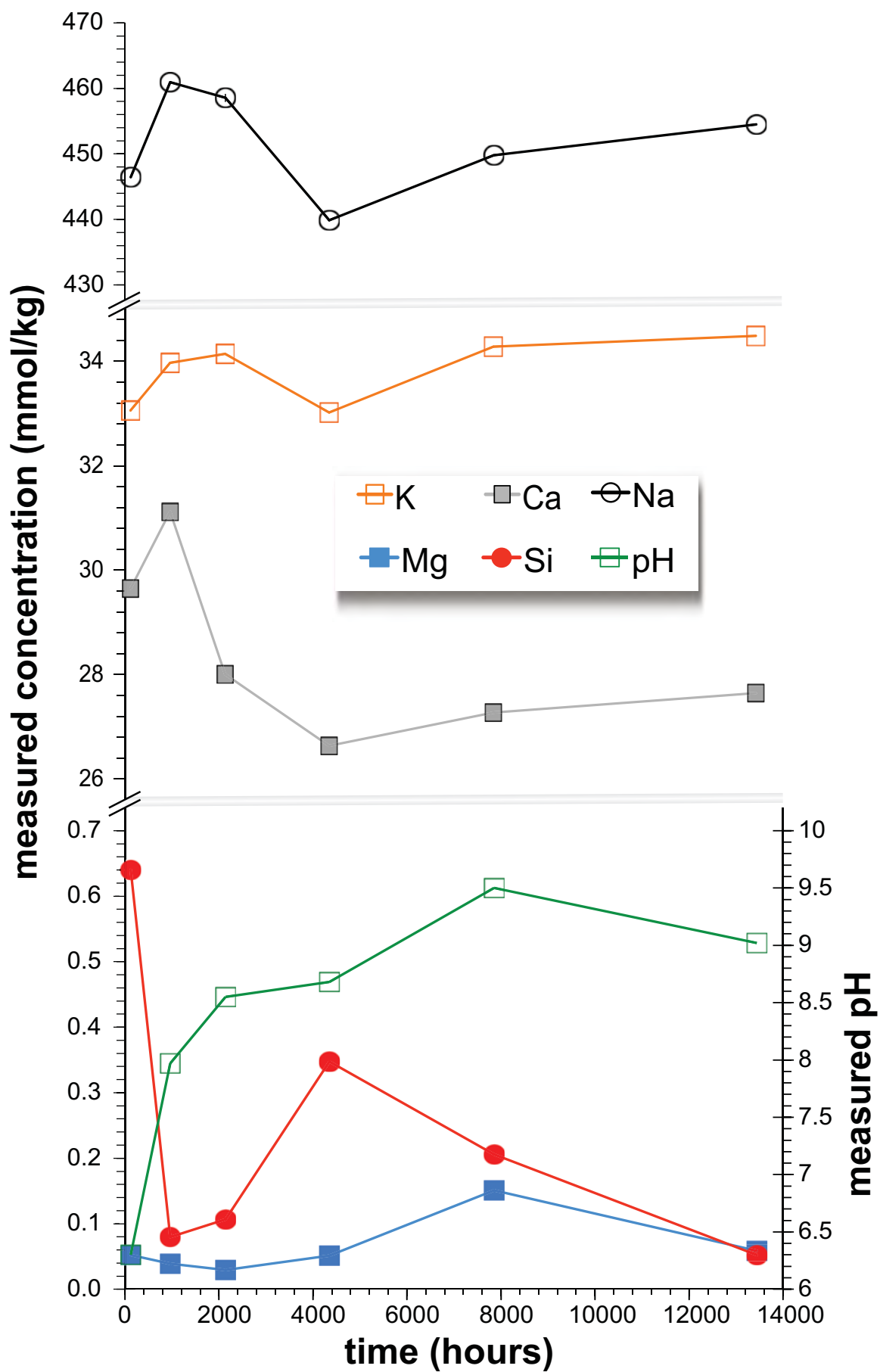
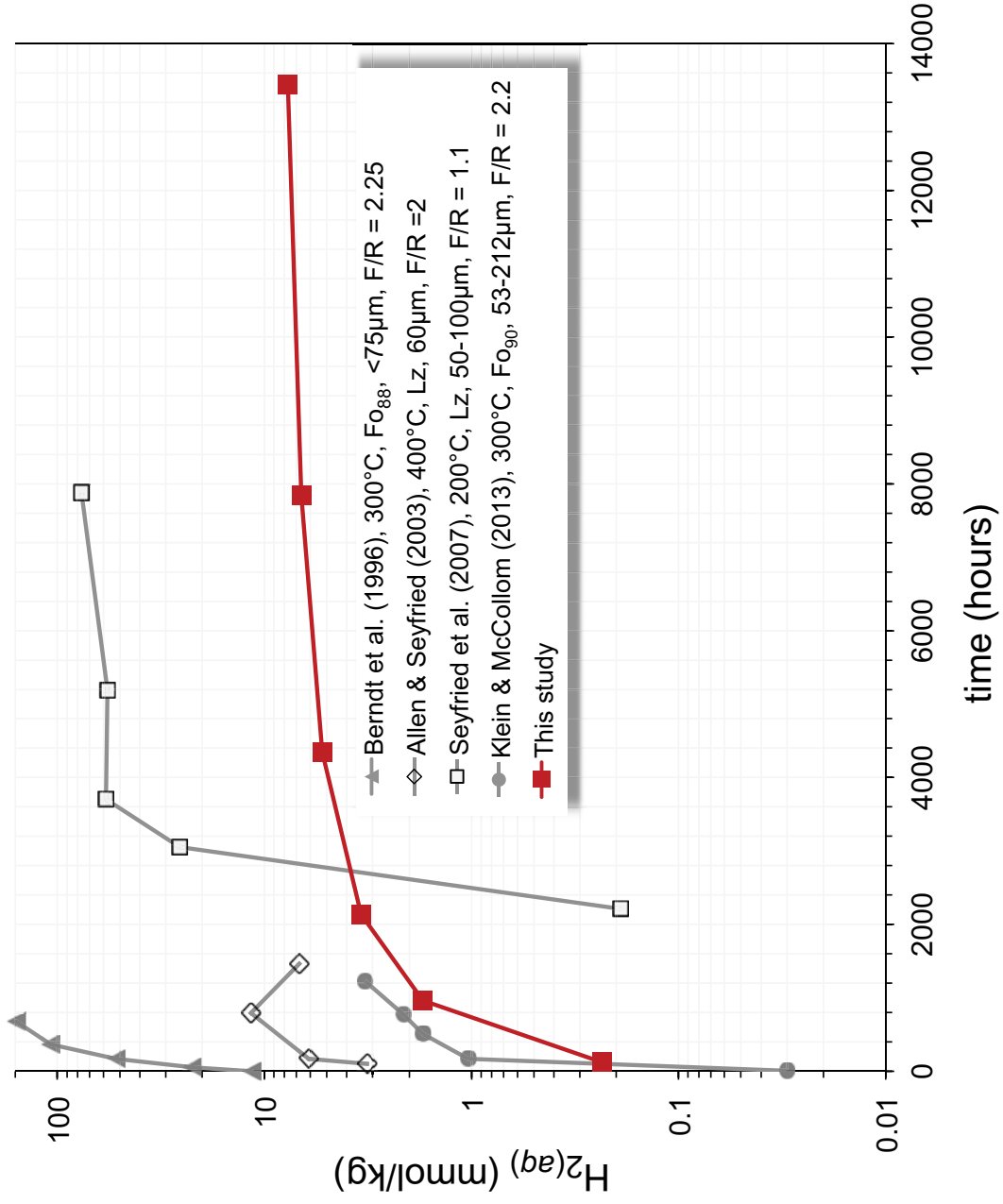


Figure 2



**Figure 3**





**Figure 4**

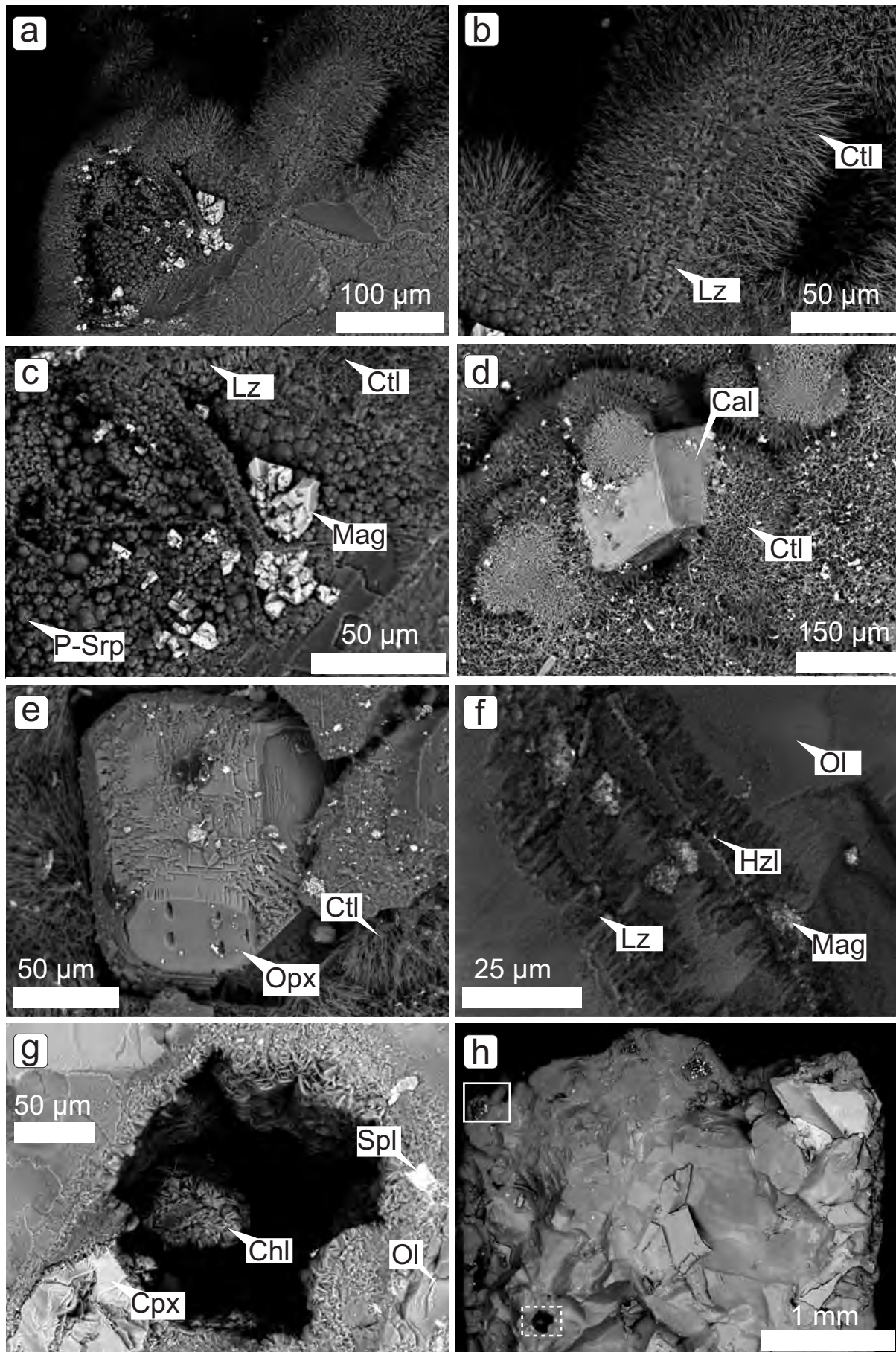
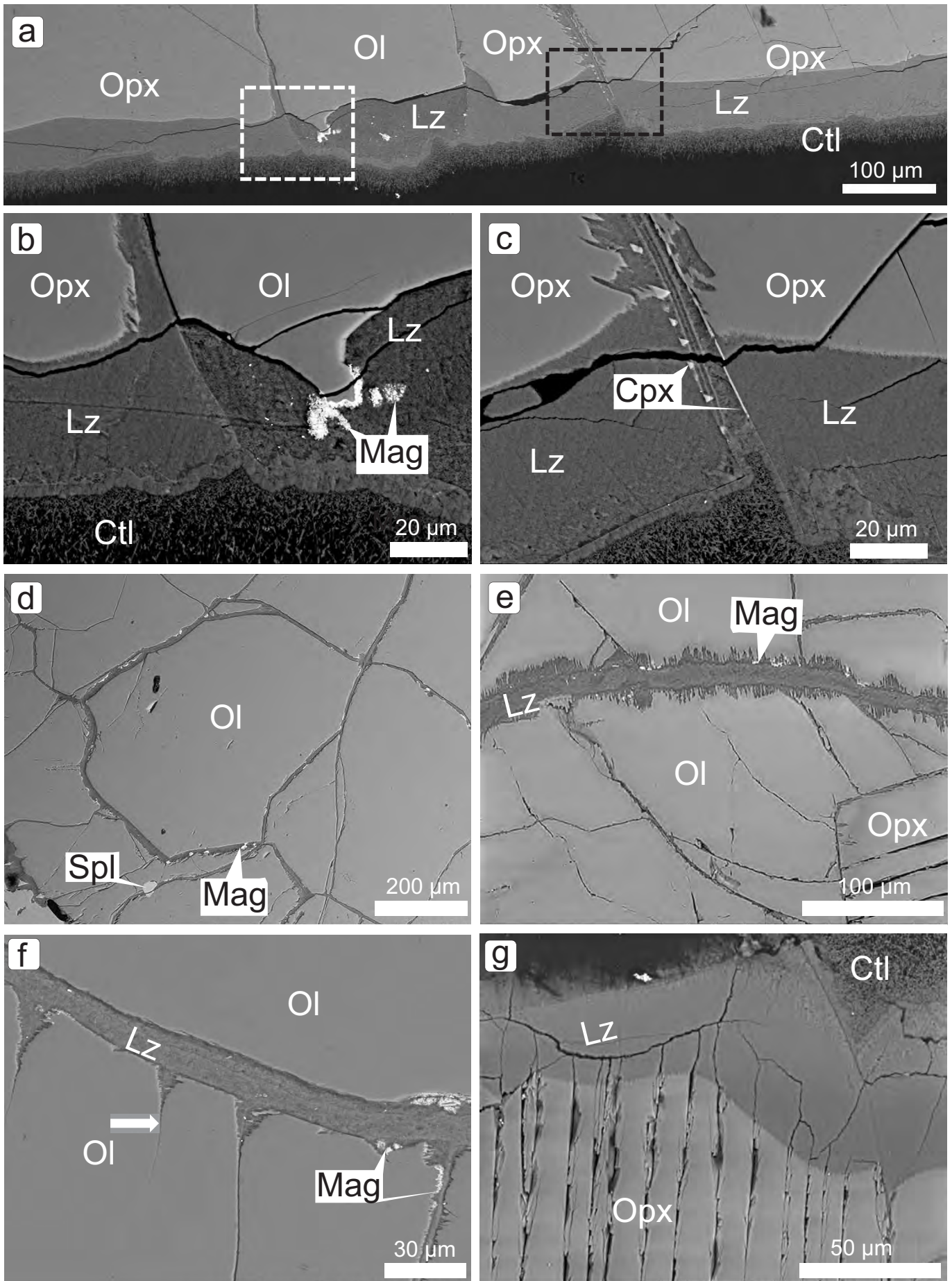


Figure 5



**Figure 6**

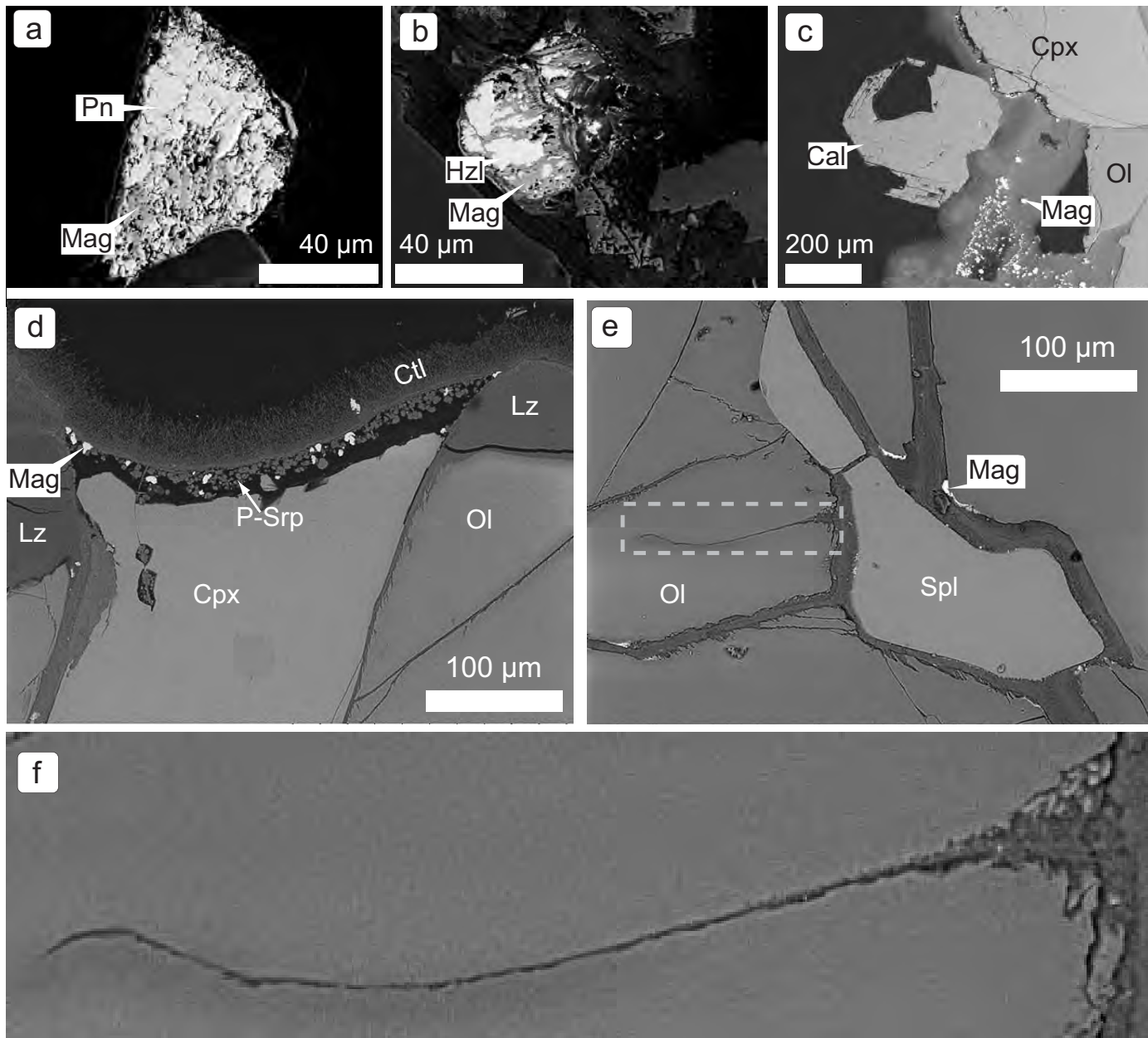
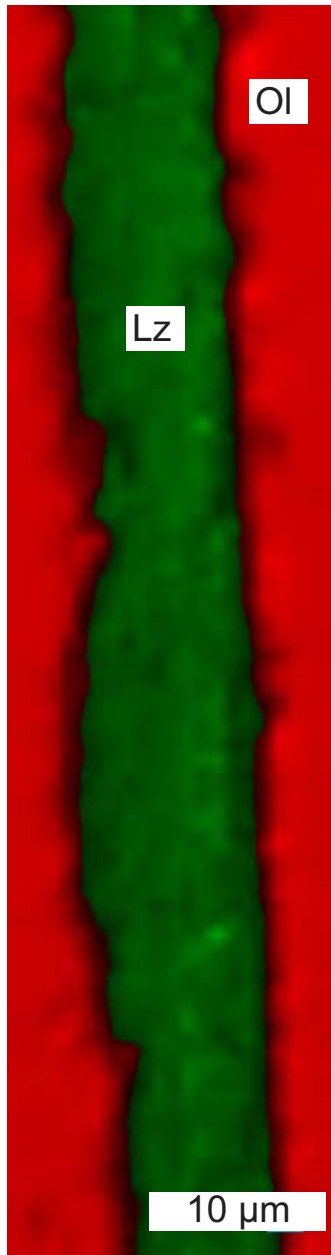


Figure 7



**Figure 8**

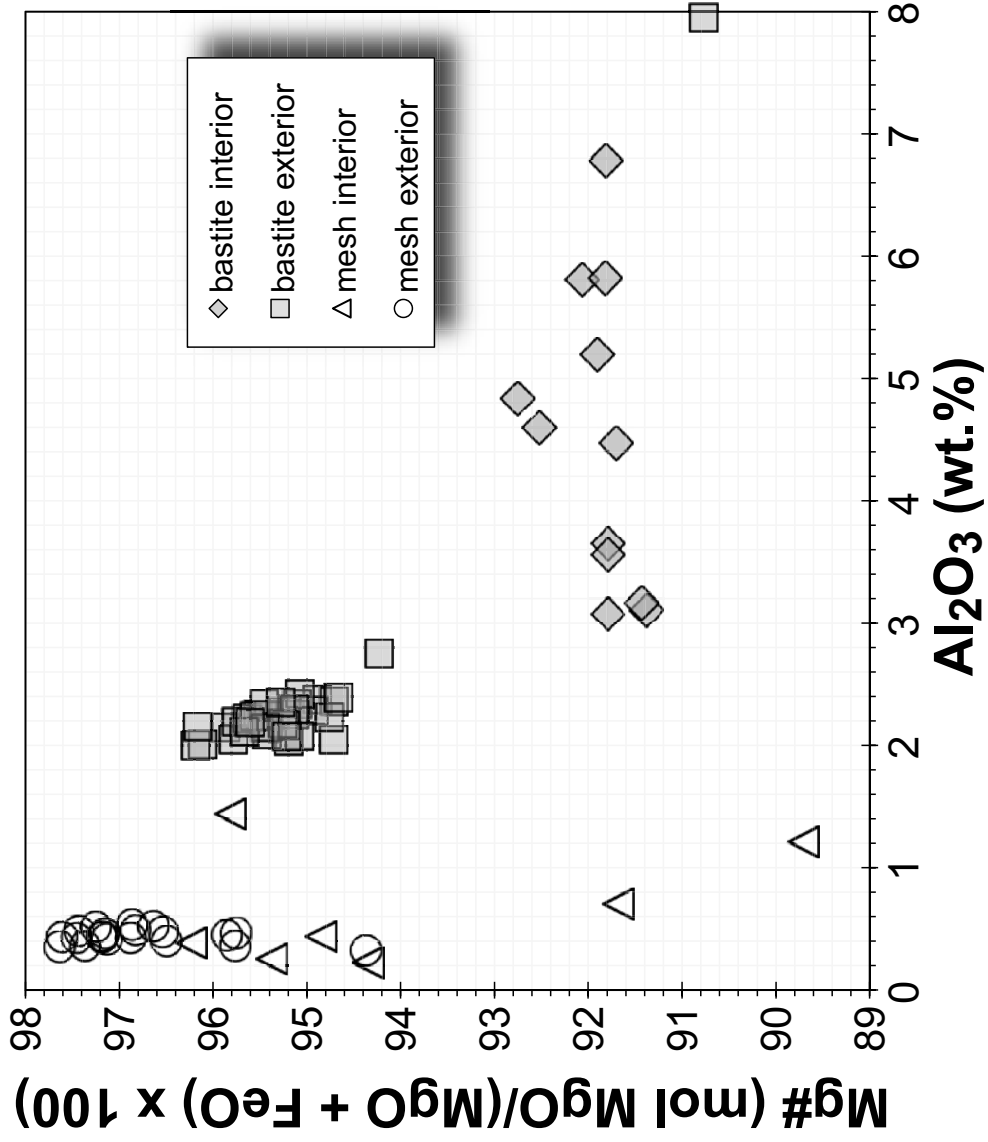


Figure 9

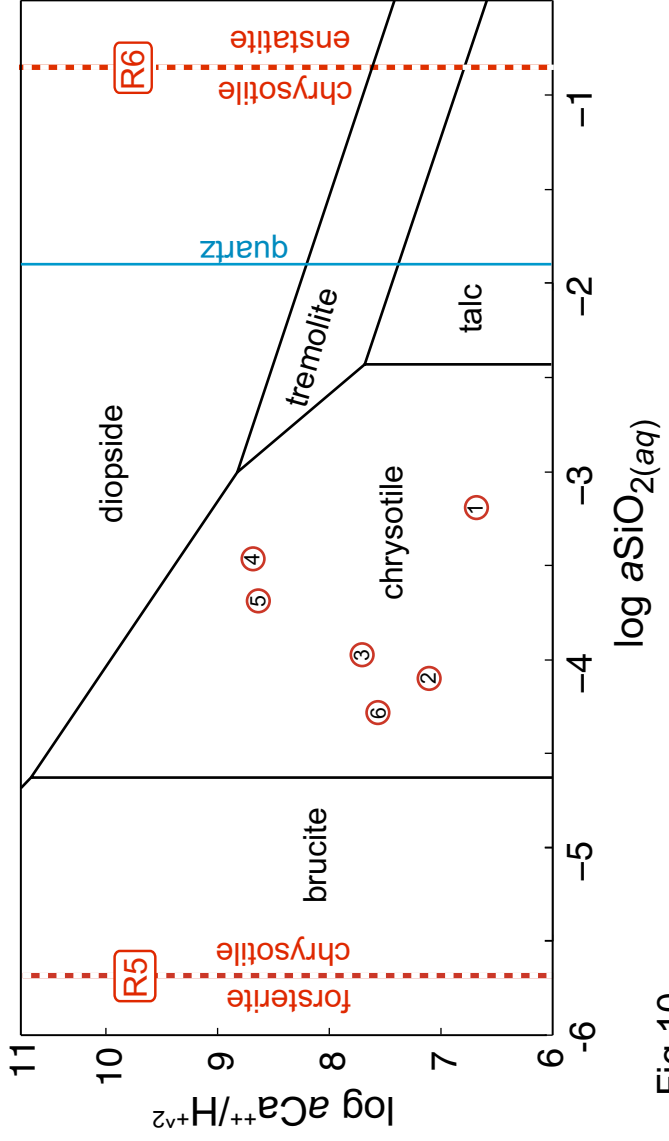


Fig 10

**Table 1:** Geochemical composition of harzburgite used as the starting material

	wt.%
<b>SiO<sub>2</sub></b>	44.66
<b>TiO<sub>2</sub></b>	0.01
<b>Al<sub>2</sub>O<sub>3</sub></b>	1.01
<b>FeO*</b>	7.67
<b>MnO</b>	0.12
<b>MgO</b>	45.96
<b>CaO</b>	0.65
<b>Na<sub>2</sub>O</b>	0.04
<b>K<sub>2</sub>O</b>	b.d.
<b>P<sub>2</sub>O<sub>5</sub></b>	0.02
<b>Sum</b>	100.15

selected trace elements (  $\mu\text{g/g}$  )

<b>Ni</b>	2404
<b>Cr</b>	2101
<b>V</b>	25
<b>Ba</b>	6
<b>Sr</b>	13
<b>Cu</b>	11
<b>Zn</b>	48

\* Total Fe calculated as FeO



**Table 2:** Electron microprobe analyses of primary minerals (wt.%)

	Ol	$\sigma$	Opx	$\sigma$	Cpx	$\sigma$	Amp	$\sigma$
# analyses	6		3		8		4	
SiO <sub>2</sub>	41.13	0.29	56.76	0.29	53.49	0.53	43.46	0.09
TiO <sub>2</sub>	0.01	0.02	0.02	0.04	0.08	0.06	0.32	0.10
Al <sub>2</sub> O <sub>3</sub>	0.01	0.01	2.96	0.23	3.52	0.15	14.83	0.05
Cr <sub>2</sub> O <sub>3</sub>	0.01	0.02	0.34	0.02	0.60	0.06	1.48	0.08
FeO	8.67	0.15	6.10	0.14	2.85	0.09	4.10	0.07
MnO	0.12	0.05	0.15	0.02	0.05	0.03	0.06	0.05
MgO	49.96	1.39	34.39	0.30	16.92	0.29	18.47	0.13
NiO	0.37	0.03	0.07	0.01	0.05	0.03	0.11	0.02
CoO	0.03	0.02	0.01	0.01	0.03	0.02	b.d.	
CaO	0.08	0.05	0.56	0.10	22.31	0.28	11.52	0.05
Na <sub>2</sub> O	n.a.		0.04	0.01	0.86	0.03	2.89	0.01
K <sub>2</sub> O	n.a.		b.d.		b.d.		1.09	0.00
Cl	n.a.		n.a.		n.a.		0.19	0.00
sum	100.38		101.39		100.76		98.54	

Ol = olivine, Opx = orthopyroxene, Cpx = clinopyroxene, Amp = amphibole, b.d. = below detection, n.a. = not analyzed

**Table 3:** Measured composition of fluid samples taken during the experiment

Sample	Time (hours)	Na (mmol/kg)	K (mmol/kg)	Ca (mmol/kg)	Mg (mmol/kg)	Si (mmol/kg)	H2 (mmol/kg)	pH	fluid (g)
starting fluid	-	463	34.0	31.1	n.d.	n.d.	n.d.	n.d.	-
bleed	0	439.6	32.4	30.5	0.03	n.d.	0.0	n.d.	43.15
	1 122	446.5	33.1	29.7	0.05	0.64	0.2	6.3	37.35
	2 963	460.9	34.0	31.1	0.04	0.08	1.7	8	34.4
	3 2138	458.6	34.1	28.0	0.03	0.11	3.4	8.6	31.01
	4 4348	439.9	33.0	26.6	0.05	0.35	5.3	8.7	27.26
	5 7850	449.8	34.3	27.3	0.15	0.21	6.6	9.5	23.17
	6 13441	454.5	34.5	27.6	0.06	0.05	7.7	9	18.34

n.d. = not determined

---

**Table 4:** Summary of petrographic observations

Primary mineral	Secondary mineral	Texture	Comments
Ol	Srp/Mag, Hzl?	mesh	Ol shows dissolution features and fractures. Intra- and transgranular veins composed of Lz, minor Mag, and traces of Hzl. Ctl and Mag after Ol are sub- to euhedral on rock exterior surface.
Opx	Srp, Chl	bastite	Opx shows etch pits, intra- and transgranular veins composed of Lz and Chl.
Spl	-	-	Spl appears unaltered.
Cpx	-	-	Cpx appears unaltered.
Po / Pn	Hzl/Mag	-	Sulfides are irregularly distributed.
Amp	Chl	-	Amp appears mostly unaltered. In some cases it appears to be replaced by Chl
-	Cal	-	Sub- to euhedral Cal precipitates exclusively on exterior rock surface.

Mineral and mineral group abbreviations after Whitney and Evans (2010)

**Table 5:** *Electron microprobe analyses of reaction products (in wt.%)*

	<b>mesh exterior</b>	<b><math>\sigma</math></b>	<b>bastite exterior</b>	<b><math>\sigma</math></b>	<b>mesh interior</b>	<b><math>\sigma</math></b>	<b>bastite interior</b>
<b># analyses</b>	<b>10</b>		<b>36</b>		<b>4</b>		<b>7</b>
SiO <sub>2</sub>	40.90	0.49	38.76	0.72	39.90	1.21	37.81
TiO <sub>2</sub>	0.02	0.03	0.04	0.05	0.02	0.03	0.02
Al <sub>2</sub> O <sub>3</sub>	0.45	0.06	2.38	0.97	0.44	0.20	5.05
Cr <sub>2</sub> O <sub>3</sub>	0.02	0.02	0.38	0.06	0.03	0.04	0.31
FeO <sup>†</sup>	2.60	0.66	3.53	0.55	4.22	1.32	5.14
MnO	0.04	0.03	0.07	0.03	0.08	0.04	0.09
MgO	40.32	0.33	39.36	1.02	39.12	1.86	33.54
NiO	0.41	0.12	0.11	0.04	0.18	0.08	0.11
CoO	0.02	0.02	0.02	0.02	0.04	0.04	0.02
SO <sub>3</sub>	0.08	0.03	0.04	0.02	0.06	0.03	0.11
CaO	0.07	0.02	0.17	0.02	0.11	0.05	0.37
Na <sub>2</sub> O	0.07	0.02	0.08	0.02	0.04	0.02	0.25
K <sub>2</sub> O	0.02	0.01	0.03	0.01	0.03	0.02	0.13
F	0.01	0.01	0.01	0.01	0.05	0.03	0.02
Cl	0.19	0.07	0.32	0.05	0.18	0.07	0.12
H <sub>2</sub> O*	14.78	0.68	14.71	0.65	15.51	2.36	16.92

	<b>heazlewoodite</b>	<b><math>\sigma</math></b>	<b>pentlandite</b>	<b><math>\sigma</math></b>		<b>calcite</b>	<b><math>\sigma</math></b>
<b># analyses</b>	<b>5</b>		<b>4</b>			<b>7</b>	
Cr	0.05	0.03	0.03	0.03	MnO	b.d.	-
Mn	b.d.	-	0.01	0.01	MgO	0.04	0.02
Co	0.30	0.04	0.68	0.04	SiO <sub>2</sub>	b.d.	-
Cu	0.10	0.02	0.19	0.03	FeO	0.02	0.02

Mg	0.05	0.01	0.04	0.01	CaO	56.54	0.40
Si	0.02	0.01	0.02	0.02	CO <sub>2</sub> *	43.4	0.39
Ti	0.02	0.02	0.04	0.02			
Fe	3.08	0.83	28.33	0.15			
Ni	70.2	0.40	36.5	0.19			
Ca	0.02	0.01	b.d.	-			
S	26.29	0.08	32.59	0.29			
Pt	0.01	0.01	0.01	0.01			
P	0.01	0.01	0.01	0.01			
Sum	100.15	0.49	98.45	0.53			

---

† total Fe calculated as FeO, \*calculated by difference, b.d. = below detection limit

---

$\sigma$	chlorite	$\sigma$
1.23	34.73	1.14
0.03	0.15	0.14
1.01	10.93	0.61
0.23	0.03	0.03
0.24	6.53	0.26
0.02	0.12	0.06
0.61	32.14	0.65
0.05	0.14	0.01
0.03	0.06	0.05
0.03	0.03	0.02
0.16	0.16	0.02
0.17	0.08	0.03
0.06	0.30	0.31
0.04	0.02	0.03
0.05	0.22	0.07
1.42	14.36	1.52